Applied Mathematical Modelling 34 (2010) 92–121

Contents lists available at ScienceDirect

Applied Mathematical Modelling

journal homepage: www.elsevier.com/locate/apm

Numerical damage assessment of Haghia Sophia bell tower by nonlinear FE modeling

Alemdar Bayraktar [a], Abdurrahman Şahin [a,*], D. Mehmet Özcan [a], Faruk Yildirim [b]

[a] Karadeniz Technical University, Department of Civil Engineering, 61080 Trabzon, Turkey
[b] Karadeniz Technical University, Geodesy and Photogrammetry Engineering, 61080 Trabzon, Turkey

ARTICLE INFO

Article history:
Received 21 December 2007
Received in revised form 22 March 2009
Accepted 24 March 2009
Available online 2 April 2009

Keywords:
Masonry
Finite element analysis
Nonlinear modeling
Seismic analysis
Failure behavior
Haghia Sophia bell tower

ABSTRACT

In the present paper, the numerical damage assessment of the masonry bell tower called "Haghia Sophia" in Trabzon, Turkey is performed by nonlinear 3D finite element modeling. The behavior of bell tower is determined under several different conditions: nonlinear static analysis containing dead and wind loads and nonlinear seismic analysis. In addition to, an assessment of the tower's stability with respect to the tilt of the tower is carried out by means of a nonlinear analysis. In the nonlinear dynamic analysis, the east–west component of 1992 Erzincan earthquake is used. Cracking and crushing of the masonry have been taken into account, as well as the influence of material nonlinearity. The numerical analysis has given a valuable picture of possible damage evolution, providing useful hints for the prosecution of structural monitoring. The displacement and stress fields, as well as the distribution of cracking have been calculated and compared to the actual distribution of fractures in the tower. It is seen from the numerical results that there is a good agreement with present damages of the bell tower.

1. Introduction

The monastery church of Haghia Sophia in Trabzon has been mentioned by many travelers, from Julien Bordier in the early seventeenth century onwards; in spite of many change to use – to mosque, military depot, cholera hospital, mosque again and now museum – it stands today, virtually unaltered since its construction in the thirteenth century, on its smooth grassy plateau looking northwards over the blue–grey stretches of the Black Sea.

As with so many Byzantine buildings, it is very difficult to establish facts concerning its history, especially with regard to the earlier periods. In 1960 the Evkaf, the Turkish Department of Religious Foundations, took it over and extensively repaired and renewed the structure, including rebuilding the wall between the south porch and naos. A new mosque has been built for the local congregation and Haghia Sophia is now secularized and open for any-one to see.

The church and bell tower are masonry structures. Masonry is probably the oldest building material that still finds wide use in today's building industries. Important new developments in masonry materials and applications occurred in the last decades but the techniques to assemble bricks and blocks are essentially the same as the ones developed some thousand years ago. Naturally, innumerable variations of masonry materials, techniques and applications occurred during the course of time. The influence factors were mainly the local culture and wealth, the knowledge of materials and tools, the availability of material and architectural reasons.

* Corresponding author. Tel.: +90 462 377 40 20; fax: +90 462 377 26 06.
E-mail addresses: alemdar@ktu.edu.tr (A. Bayraktar), abdurrahmansahin@hotmail.com (A. Şahin), mozcan@ktu.edu.tr (D.M. Özcan), yfaruk@ktu.edu.tr (F. Yildirim).

0307-904X/$ - see front matter Crown Copyright © 2009 Published by Elsevier Inc. All rights reserved.
doi:10.1016/j.apm.2009.03.033

The most important characteristic of masonry construction is its simplicity. Laying pieces of stone or bricks on top of each other, either with or without cohesion via mortar, is a simple, though adequate technique that has been successful ever since remote ages. Other important characteristics are the aesthetics, solidity, durability and low maintenance, versatility, sound absorption and fire protection. Loadbearing walls, infill panels to resist seismic and wind loads, prestressed masonry cores and low–rise buildings are examples of constructions where the use of structural masonry is presently competitive. However, innovative applications of structural masonry are hindered by the fact that the development of design rules has not kept pace with the developments for concrete and steel. The underlying reason is the lack of insight and models for the complex behavior of units, mortar, joints and masonry as a composite material. Existing calculation methods are mainly of empirical and traditional nature and the use of numerical tools for the analysis or design of masonry structures is rather incipient.

Masonry is a material which exhibits distinct directional properties due to the mortar joints which act as planes of weakness. In general, the approach towards the numerical representation of masonry can focus on the micro-modeling of the individual components, *viz.* unit (brick, block, etc.) and mortar, or the macro-modeling of masonry as a composite [1]. Depending on the level of accuracy and the simplicity desired, it is possible to use the following modeling strategies (Fig. 1),

- Micro-modeling
  - Detailed micro-modeling – units and mortar in the joints are represented by continuum elements whereas the unit-mortar interface is represented by discontinuous elements;
  - Simplified micro-modeling – expanded units are represented by continuum elements whereas the behavior of the mortar joints and unit-mortar interface is lumped in discontinuous elements;
- Homogenization – replaces the complex geometry of the basic cell by a simplified geometry so that a close-form solution of the homogenization problem is possible.
- Macro-modeling – units, mortar and unit-mortar interface are smeared out in the continuum.

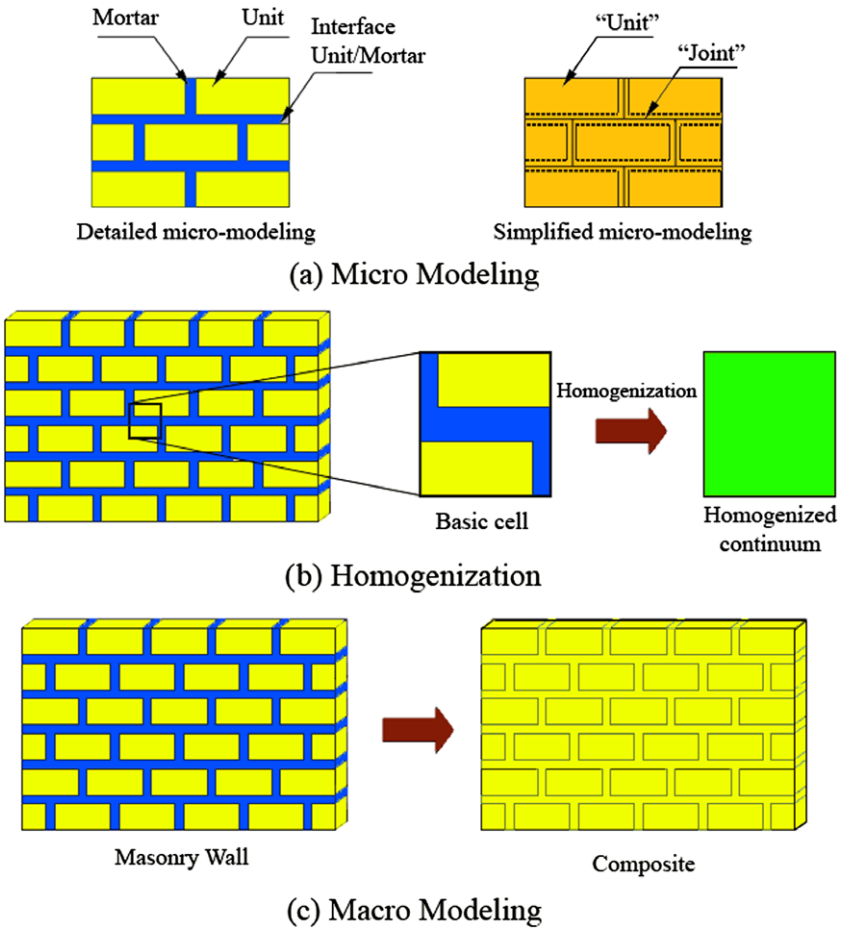

Fig. 1. Modeling strategies for masonry structures.

In detailed micro-modeling approach, Young's modulus, Poisson's ratio and, optionally, inelastic properties of both unit and mortar are taken into account. The interface represents a potential crack/slip plane with initial dummy stiffness to avoid interpenetration of the continuum. This enables the combined action of unit, mortar and interface to be studied under a magnifying glass. In simplified micro-modeling approach, each joint, consisting of mortar and the two unit-mortar interfaces, is lumped into an "average" interface while the units are expanded in order to keep the geometry unchanged. Masonry is thus considered as a set of elastic blocks bonded by potential fracture/slip lines at the joints. Accuracy is lost since Poisson's effect of the mortar is not included.

The homogenization techniques shown in Fig. 1, which permit to establish constitutive relations in terms of averaged stresses and strains from the geometry and constitutive relations of the individual components, can represent a step forward in masonry modeling, mostly because of the possibility to use standard material models and software codes for isotropic materials. Despite the complexity of masonry, much information can be gained from the study of regular masonry structures, in which a periodic repetition of the microstructure occurs due to a constant arrangement of the units (or constant bond). The most popular homogenization approach replaces the complex geometry of the basic cell by a simplified geometry so that a close-form solution of the homogenization problem is possible [2,3]. The homogenization has generally been performed in two steps, head (or vertical) and bed (or horizontal) joints being introduced successively. The use of two separate homogenization steps does not explicitly account for the regular offset of vertical mortar joints belonging to two consecutive layered unit courses, which results in significant errors in the case of nonlinear analysis.

Macro-modeling approach does not make a distinction between individual units and joints but treats masonry as a homogeneous anisotropic continuum. Macro-models are applicable when the structure is composed of solid walls with sufficiently large dimensions so that the stresses across or along a macro-length will be essentially uniform. Clearly, macro-modeling is more practice oriented due to the reduced time and memory requirements as well as a user-friendly mesh generation. This type of modeling is most valuable when a compromise between accuracy and efficiency is needed. There are valuable studies about macro-modeling.

There are many studies about micro-modeling [4,5], homogenization [6–13] and macro-modeling [14–16] techniques. The detailed investigations about masonry modeling techniques may be found in [17].

Because historical buildings are considered to have large dimensions, the focus will be on the macro-modeling of masonry. The intention is not to go interaction between stone and mortar. Target is to use existing models as a tool to distinct the safe from the unsafe region within the constraint of an acceptable accuracy and efficiency.

In literature review, we can see that most of big historical structures has been modeled with macro-modeling strategy. Buti's bell tower in Italy has been studied by Bernardeschi et al. [18]. They have used two different analyses, firstly the bell tower subjected to its own weight alone, and then structure subjected to both its own weight and a horizontal load, which models a seismic action. They investigated crack distribution numerically and had a good agreement with the actual distribution.

Eighth-century masonry tower called "Torre Sineo" (Alba, Italy) is described, analyzed and monitored by Carpinteri et al. [19]. In that study, the building has been analyzed and monitored because of an emerging damage pattern, and also some seismic events during the last few years.

The analysis performed for the characterization of the dynamic structural behavior of the bell tower of "Nuestra Sra. de la Misericordia Church" (Valencia, Spain) by Ivorra and Pallares [20]. Subsequent to the geometrical analysis of the bell tower structure, different numerical models were calibrated based on dynamic tests to determine the bending and torsion frequencies of the tower.

A presentation is given of the fundamental design choices and of the selection of the most appropriate materials and techniques which have been made for strengthening the Monza cathedral bell tower by Modena et al. [21]. The investigation carried out on site and in the laboratory on the materials and structure of Monza bell tower allows the detection of the details of damage, which is evolving toward the failure.

Seismic analysis of the Asinelli Tower in Bologna (Italy) has been studied by Riva et al. [22]. In this study, an assessment of the tower's stability with respect to compatible seismic events with the region seismicity is carried out by means of a nonlinear dynamic analysis on a simplified model.

The application of georadar to the detection of three main structural problems for the bell tower (Torrazzo) of Cremona is studied by Binda et al. [23]. Their study demonstrates the necessity and the potential of a multidisciplinary collaboration for the solution of morphological and diagnostic problems by use of non-destructive investigations.

A case study is fully detailed, including the aspects of historical, damage and geometric investigations, of advanced numerical analysis, of justification of remedial measures and of detailing the adopted strengthening of Outeiro Church in Portugal by Lourenço [24]. In addition to these, many useful studies have been done about old historical structures [25–29].

In this paper, numerical damage assessment of Haghia Sophia masonry bell tower in Trabzon, Turkey is determined by using the finite element code ANSYS [30]. The macro-modeling technique is considered in the nonlinear 3D static analysis including dead and wind loads and seismic analysis.

2. The numerical formulations

For modeling masonry, ANSYS concrete material model is used because ANSYS concrete material model has the most similar behavior with masonry and by this modeling cracking and crushing situations can be observed.

Difficulties of conceiving and implementing macro-models for the analysis of masonry structures arise especially due to the intrinsic complexity of formulating anisotropic inelastic behavior. As a rule, it is not possible to study masonry with isotropic concrete like models because of the anisotropic behavior of masonry at failure [6,7,17,31,32]. Anisotropic models are rarely available in commercial codes and therefore it is commonly accepted that isotropic averaged quantities are used in applications [18–29]. In spite of this limitation, in the authors' opinion, the concrete model has proven to be able to reasonably predict the masonry behavior as long as proper material definition is provided.

In this section, the nonlinear material model used in this study is explained, the mathematical formulations of nonlinear cracking modeling of the concrete material are explained and the general mathematical formulations of static analysis, modal analysis and transient analysis used in this study are explained, respectively. The Newton–Raphson method used in the overall nonlinear analysis of bell tower is also explained. All theoretical formulations presented here follow ANSYS theory [33]. The detailed discussions of these mathematical formulations may be found in [33].

2.1. Mathematical model of concrete material

The concrete material model predicts the failure of brittle materials. Both cracking and crushing failure modes are accounted for.

The criterion for failure of concrete due to a multiaxial stress state can be expressed in the form

$$\frac{F}{f_c} - S \geqslant 0, \tag{1}$$

where:

F = a function (to be discussed) of the principal stress state ($\sigma_{xp}, \sigma_{yp}, \sigma_{zp}$);
S = failure surface (to be discussed) expressed in terms of principal stresses and five input parameters f_t, f_c, f_{cb}, f_1 and f_2 defined in Table 1;
f_c = uniaxial crushing strength;
$\sigma_{xp}, \sigma_{yp}, \sigma_{zp}$ = principal stresses in principal directions.

If Eq. (1) is not satisfied, there is no attendant cracking or crushing. Otherwise, the material will crack if any principal stress is tensile while crushing will occur if all principal stresses are compressive.

A total of five input strength parameters (each of which can be temperature dependent) are needed to define the failure surface as well as an ambient hydrostatic stress state. These are presented in Table 1.

However, the failure surface can be specified with a minimum of two constants, f_t and f_c. The other three constants default to Willam and Warnke [34]:

$$f_{cb} = 1.2 f_c, \tag{2}$$
$$f_1 = 1.45 f_c, \tag{3}$$
$$f_2 = 1.725 f_c. \tag{4}$$

However, these default values are valid only for stress states where the condition

$$|\sigma_h| \leqslant \sqrt{3} f_c, \tag{5}$$
$$\left(\sigma_h = \text{hydrostatic stress state} = \frac{1}{3}(\sigma_{xp} + \sigma_{yp} + \sigma_{zp})\right) \tag{6}$$

is satisfied. Thus condition (5) applies to stress situations with a low hydrostatic stress component. All five failure parameters should be specified when a large hydrostatic stress component is expected. If condition (5) is not satisfied and the default values shown in Eqs. (2)–(4) are assumed, the strength of the concrete material may be incorrectly evaluated.

Both the function F and the failure surface S are expressed in terms of principal stresses denoted as σ_1,σ_2 and σ_3 where:

$$\sigma_1 = \max(\sigma_{xp}, \sigma_{yp}, \sigma_{zp}), \tag{7}$$
$$\sigma_3 = \min(\sigma_{xp}, \sigma_{yp}, \sigma_{zp}) \tag{8}$$

Table 1
Concrete material model representing masonry for bell tower.

Label	Description	Value (MPa)
f_t	Ultimate uniaxial tensile strength	0.2
f_c	Ultimate uniaxial compressive strength	2
f_{cb}	Ultimate biaxial compressive strength	2.4
σ_h^a	Ambient hydrostatic stress state	3.4641
f_1	Ultimate compressive strength for a state of biaxial compression superimposed on hydrostatic stress state σ_h^a	2.9
f_2	Ultimate compressive strength for a state of uniaxial compression superimposed on hydrostatic stress state σ_h^a	3.45

and $\sigma_1 \geqslant \sigma_2 \geqslant \sigma_3$. The failure of concrete is categorized into four domains:

1. $0 \geqslant \sigma_1 \geqslant \sigma_2 \geqslant \sigma_3$ (Compression–compression–compression)
2. $\sigma_1 \geqslant 0 \geqslant \sigma_2 \geqslant \sigma_3$ (Tensile–compression–compression)
3. $\sigma_1 \geqslant \sigma_2 \geqslant 0 \geqslant \sigma_3$ (Tensile–tensile–compression)
4. $\sigma_1 \geqslant \sigma_2 \geqslant \sigma_3 \geqslant 0$ (Tensile–tensile–tensile)

In each domain, independent functions describe F and the failure surface S. The four functions describing the general function F are denoted as F_1, F_2, F_3 and F_4 while the functions describing S are denoted as S_1, S_2, S_3 and S_4. The functions S_i ($i = 1,4$) have the properties that the surface they describe is continuous while the surface gradients are not continuous when anyone of the principal stresses changes sign. The surface will be shown in Figs. 2 and 4. These functions are discussed in detail below for each domain [33].

2.1.1. The domain $0 \geqslant \sigma_1 \geqslant \sigma_2 \geqslant \sigma_3$

In the compression–compression–compression regime, the failure criterion of Willam and Warnke is implemented. In this case, F takes the form

$$F = F_1 = \frac{1}{\sqrt{15}}\left[(\sigma_1 - \sigma_2)^2 + (\sigma_2 - \sigma_3)^2 + (\sigma_3 - \sigma_1)^2\right]^{\frac{1}{2}} \tag{9}$$

and S is defined as

$$S = S_1 = \frac{2r_2(r_2^2 - r_1^2)\cos\eta + r_2(2r_1 - r_2)[4(r_2^2 - r_1^2)\cos^2\eta + 5r_1^2 - 4r_1r_2]^{\frac{1}{2}}}{4(r_2^2 - r_1^2)\cos^2\eta + (r_2 - 2r_1)^2}. \tag{10}$$

Terms used to define S are:

$$\cos\eta = \frac{2\sigma_1 - \sigma_2 - \sigma_3}{\sqrt{2}\left[(\sigma_1 - \sigma_2)^2 + (\sigma_2 - \sigma_3)^2 + (\sigma_3 - \sigma_1)^2\right]^{\frac{1}{2}}}, \tag{11}$$

$$r_1 = a_0 + a_1\xi + a_2\xi^2, \tag{12}$$

$$r_2 = b_0 + b_1\xi + b_2\xi^2, \tag{13}$$

$$\xi = \frac{\sigma_h}{f_c},$$

σ_h is defined by Eq. (6) and the undetermined coefficients a_0, a_1, a_2, b_0, b_1 and b_2 are discussed below.

This failure surface is shown as Fig. 2. The angle of similarity η describes the relative magnitudes of the principal stresses. From Eq. (11), $\eta = 0°$ refers to any stress state such that $\sigma_3 = \sigma_2 > \sigma_1$ (e.g. uniaxial compression, biaxial tension) while $\xi = 60°$ for any stress state where $\sigma_3 > \sigma_2 = \sigma_1$ (e.g. uniaxial tension, biaxial compression). All other multiaxial stress states have angles of similarity such that $0° \leqslant \eta \leqslant 60°$. When $\eta = 0°$, S_1 (Eq. (10)) equals r_1 while if $\eta = 60°$, S_1 equals r_2. Therefore, the function r_1 represents the failure surface of all stress states with $\eta = 0°$. The functions r_1, r_2 and the angle η are depicted in Fig. 2.

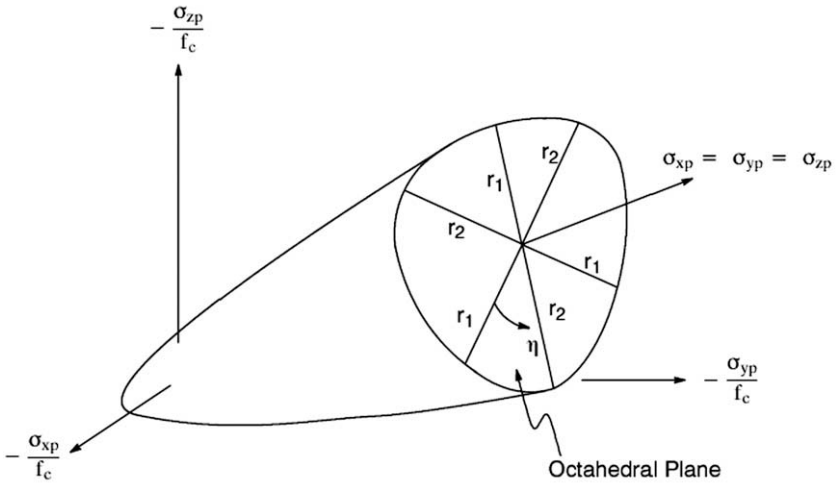

Fig. 2. 3-D Failure surface in principal stress space [33].

It may be seen that the cross-section of the failure plane has cyclic symmetry about each 120° sector of the octahedral plane due to the range $0^\circ \leqslant \eta \leqslant 60^\circ$ of the angle of similitude. The function r_1 is determined by adjusting a_0,a_1 and a_2 such that f_t, f_{cb} and f_1 all lie on the failure surface. The proper values for these coefficients are determined through solution of the simultaneous equations:

$$\begin{Bmatrix} \frac{F_1}{f_c}(\sigma_1 = f_t,\ \sigma_2 = \sigma_3 = 0) \\ \frac{F_1}{f_c}(\sigma_1 = 0,\ \sigma_2 = \sigma_3 = -f_{cb}) \\ \frac{F_1}{f_c}(\sigma_1 = -\sigma_h^a,\ \sigma_2 = \sigma_3 = -\sigma_h^a - f_1) \end{Bmatrix} = \begin{bmatrix} 1 & \xi_t & \xi_t^2 \\ 1 & \xi_{cb} & \xi_{cb}^2 \\ 1 & \xi_1 & \xi_1^2 \end{bmatrix} \begin{Bmatrix} a_0 \\ a_1 \\ a_2 \end{Bmatrix}, \tag{14}$$

with

$$\xi_t = \frac{f_t}{3f_c}, \quad \xi_{cb} = -\frac{2f_{cb}}{3f_c}, \quad \xi_1 = -\frac{\sigma_h^a}{f_c} - \frac{2f_1}{3f_c}. \tag{15}$$

The function r_2 is calculated by adjusting b_0, b_1, and b_2 to satisfy the conditions:

$$\begin{Bmatrix} \frac{F_1}{f_c}(\sigma_1 = \sigma_2 = 0,\ \sigma_3 = -f_c) \\ \frac{F_1}{f_c}(\sigma_1 = \sigma_2 = -\sigma_h^a,\ \sigma_3 = -\sigma_h^a - f_2) \\ 0 \end{Bmatrix} = \begin{bmatrix} 1 & -\frac{1}{3} & \frac{1}{9} \\ 1 & \xi_2 & \xi_2^2 \\ 1 & \xi_0 & \xi_0^2 \end{bmatrix} \begin{Bmatrix} b_0 \\ b_1 \\ b_2 \end{Bmatrix}. \tag{16}$$

ξ_2 is defined by:

$$\xi_2 = -\frac{\sigma_h^a}{f_c} - \frac{f_2}{3f_c} \tag{17}$$

and ξ_0 is the positive root of the equation

$$r_2(\xi_0) = a_0 + a_1\xi_0 + a_2\xi_0^2 = 0, \tag{18}$$

where a_0, a_1, and a_2 are evaluated by Eq. (14).

Since the failure surface must remain convex, the ratio r_1/r_2 is restricted to the range

$$0.5 < r_1/r_2 < 1.25, \tag{19}$$

although the upper bound is not considered to be restrictive since $r_1/r_2 < 1$ for most materials [35]. Also, the coefficients a_0, a_1, a_2, b_0, b_1, and b_2 must satisfy the conditions:

$$a_0 > 0, \quad a_1 \leqslant 0, \quad a_2 \leqslant 0, \tag{20}$$

$$b_0 > 0, \quad b_1 \leqslant 0, \quad b_2 \leqslant 0. \tag{21}$$

Therefore, the failure surface is closed and predicts failure under high hydrostatic pressure ($\xi > \xi_2$). This closure of the failure surface has not been verified experimentally and it has been suggested that a von Mises type cylinder is a more valid failure surface for large compressive σ_h values. Consequently, it is recommended that the values of f_1 and f_2 are selected at a hydrostatic stress level (σ_h^a) in the vicinity of or above the expected maximum hydrostatic stress encountered in the structure.

Eq. (18) expresses the condition that the failure surface has an apex at $\xi = \xi_0$. A profile of r_1 and r_2 as a function of ξ is shown in Fig. 3.

The lower curve represents all stress states such that $\eta = 0^\circ$ while the upper curve represents stress states such that $\eta = 60^\circ$. If the failure criterion is satisfied, the material is assumed to crush [33].

2.1.2. The domain $\sigma_1 \geqslant 0 \geqslant \sigma_2 \geqslant \sigma_3$

In the tension–compression–compression regime, F takes the form

$$F = F_2 = \frac{1}{\sqrt{15}}\left[(\sigma_2 - \sigma_3)^2 + \sigma_2^2 + \sigma_3^2\right]^{\frac{1}{2}} \tag{22}$$

and S is defined as

$$S = S_2 = \left(1 - \frac{\sigma_1}{f_t}\right)\frac{2p_2(p_2^2 - p_1^2)\cos\eta + p_2(2p_1 - p_2)\left[4(p_2^2 - p_1^2)\cos^2\eta + 5p_1^2 - 4p_1p_2\right]^{\frac{1}{2}}}{4(p_2^2 - p_1^2)\cos^2\eta + (p_2 - 2p_1)^2}, \tag{23}$$

where $\cos\eta$ is defined by Eq. (11) and

$$p_1 = a_0 + a_1\chi + a_2\chi^2, \tag{24}$$

$$p_2 = b_0 + b_1\chi + b_2\chi^2. \tag{25}$$

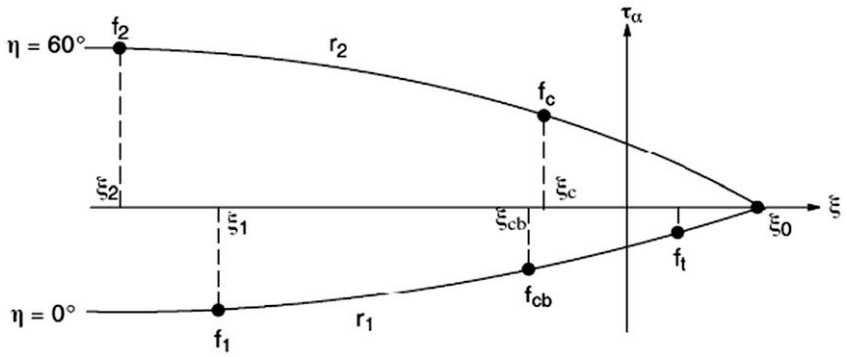

Fig. 3. A profile of the failure surface as a function of ξ_a [33].

The coefficients a_0, a_1, a_2, b_0, b_1, b_2 are defined by Eqs. (14) and (16) while

$$\chi = \frac{1}{3}(\sigma_2 + \sigma_3). \tag{26}$$

If the failure criterion is satisfied, cracking occurs in the plane perpendicular to principal stress σ_1 [33].

2.1.3. The domain $\sigma_1 \geqslant \sigma_2 \geqslant 0 \geqslant \sigma_3$

In the tension–tension–compression regime, F takes the form

$$F = F_3 = \sigma_i; \quad i = 1, 2 \tag{27}$$

and S is defined as

$$S = S_3 = \frac{f_t}{f_c}\left(1 + \frac{\sigma_3}{f_c}\right); \quad i = 1, 2. \tag{28}$$

If the failure criterion for both i = 1,2 is satisfied, cracking occurs in the planes perpendicular to principal stresses σ_1 and σ_2. If the failure criterion is satisfied only for i = 1, cracking occurs only in the plane perpendicular to principal stress σ_1 [33].

2.1.4. The domain $\sigma_1 \geqslant \sigma_2 \geqslant \sigma_3 \geqslant 0$

In the tension–tension–tension regimes, F takes the form

$$F = F_4 = \sigma_i; \quad i = 1, 2, 3 \tag{29}$$

and S is defined as

$$S = S_4 = \frac{f_t}{f_c}. \tag{30}$$

If the failure criterion is satisfied in directions 1, 2, and 3, cracking occurs in the planes perpendicular to principal stresses, σ_1, σ_2, σ_3.

If the failure criterion is satisfied in directions 1 and 2, cracking occurs in the plane perpendicular to principal stresses σ_1 and σ_2.

If the failure criterion is satisfied only in direction 1, cracking occurs in the plane perpendicular to principal stress σ_1.

Fig. 4 represents the 3-D failure surface for states of stress that are biaxial or nearly biaxial. If the most significant nonzero principal stresses are in σ_{xp} and σ_{yp} directions, the three surfaces presented are for σ_{zp} slightly greater than zero, σ_{zp} equal to zero, and σ_{zp} slightly less than zero. Although the three surfaces, shown as projections on the $\sigma_{xp} - \sigma_{yp}$ plane, are nearly equivalent and the 3-D failure surface is continuous, the mode of material failure is a function of the sign of σ_{zp}. For example, if σ_{xp} and σ_{yp} are both negative and σ_{zp} is slightly positive, cracking would be predicted in a direction perpendicular to the σ_{zp} direction. However, if σ_{zp} is zero or slightly negative, the material is assumed to crush [33].

2.2. Mathematical modeling of a crack in concrete material

The presence of a crack at an integration point is represented through modification of the stress–strain relations by introducing a plane of weakness in a direction normal to the crack face. Also, a shear transfer coefficient β_t is introduced which

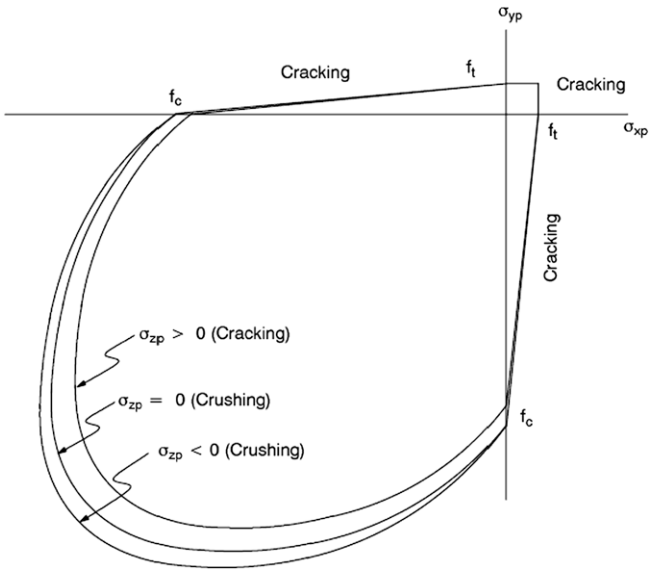

Fig. 4. Failure surface in principal stress space σ_{zp} close to zero [33].

represents a shear strength reduction factor for those subsequent loads which induce sliding (shear) across the crack face. The stress–strain relations for a material that has cracked in one direction only become:

$$[D_c^{ck}] = \frac{E}{(1+v)} \begin{bmatrix} \frac{R^t(1+v)}{E} & 0 & 0 & 0 & 0 & 0 \\ 0 & \frac{1}{1-v} & \frac{v}{1-v} & 0 & 0 & 0 \\ 0 & \frac{v}{1-v} & \frac{1}{1-v} & 0 & 0 & 0 \\ 0 & 0 & 0 & \frac{\beta_t}{2} & 0 & 0 \\ 0 & 0 & 0 & 0 & \frac{1}{2} & 0 \\ 0 & 0 & 0 & 0 & 0 & \frac{\beta_t}{2} \end{bmatrix}, \tag{31}$$

where the superscript ck signifies that the stress–strain relations refer to a coordinate system parallel to principal stress directions with the x^{ck} axis perpendicular to the crack face. R^t is the slope (secant modulus) as defined in Fig. 5. R^t works with adaptive descent and diminishes to 0.0 as the solution converges.

In Fig. 5,

f_t = uniaxial tensile cracking stress
T_c = multiplier for amount of tensile stress relaxation

If the crack closes, then all compressive stresses normal to the crack plane are transmitted across the crack and only a shear transfer coefficient β_c for a closed crack is introduced. Then $[D_c^{ck}]$ can be expressed as

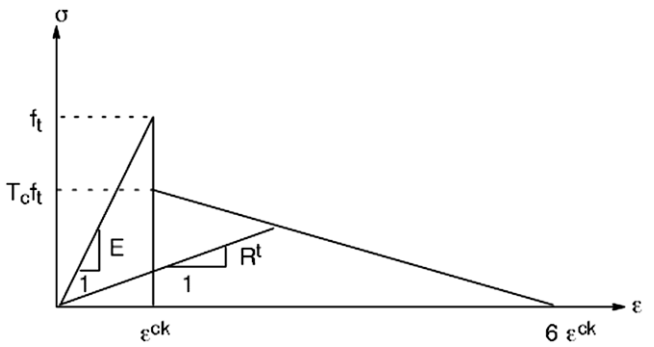

Fig. 5. Strength of cracked condition [33].

$$[D_c^{ck}] = \frac{E}{(1+v)(1-2v)} \begin{bmatrix} (1-v) & v & v & 0 & 0 & 0 \\ v & (1-v) & v & 0 & 0 & 0 \\ v & v & (1-v) & 0 & 0 & 0 \\ 0 & 0 & 0 & \beta_c \frac{1-2v}{2} & 0 & 0 \\ 0 & 0 & 0 & 0 & \frac{1-2v}{2} & 0 \\ 0 & 0 & 0 & 0 & 0 & \beta_c \frac{1-2v}{2} \end{bmatrix}. \tag{32}$$

The stress–strain relations for concrete that has cracked in two directions are:

$$[D_c^{ck}] = E \begin{bmatrix} \frac{R^t}{E} & 0 & 0 & 0 & 0 & 0 \\ 0 & \frac{R^t}{E} & 0 & 0 & 0 & 0 \\ 0 & 0 & 1 & 0 & 0 & 0 \\ 0 & 0 & 0 & \frac{\beta_t}{2(1+v)} & 0 & 0 \\ 0 & 0 & 0 & 0 & \frac{\beta_t}{2(1+v)} & 0 \\ 0 & 0 & 0 & 0 & 0 & \frac{\beta_t}{2(1+v)} \end{bmatrix}. \tag{33}$$

If both directions reclose,

$$[D_c^{ck}] = \frac{E}{(1+v)(1-2v)} \begin{bmatrix} (1-v) & v & v & 0 & 0 & 0 \\ v & (1-v) & v & 0 & 0 & 0 \\ v & v & (1-v) & 0 & 0 & 0 \\ 0 & 0 & 0 & \beta_c \frac{1-2v}{2} & 0 & 0 \\ 0 & 0 & 0 & 0 & \beta_c \frac{1-2v}{2} & 0 \\ 0 & 0 & 0 & 0 & 0 & \beta_c \frac{1-2v}{2} \end{bmatrix}. \tag{34}$$

The stress–strain relations for concrete that has cracked in all three directions are:

$$[D_c^{ck}] = E \begin{bmatrix} \frac{R^t}{E} & 0 & 0 & 0 & 0 & 0 \\ 0 & \frac{R^t}{E} & 0 & 0 & 0 & 0 \\ 0 & 0 & \frac{R^t}{E} & 0 & 0 & 0 \\ 0 & 0 & 0 & \frac{\beta_t}{2(1+v)} & 0 & 0 \\ 0 & 0 & 0 & 0 & \frac{\beta_t}{2(1+v)} & 0 \\ 0 & 0 & 0 & 0 & 0 & \frac{\beta_t}{2(1+v)} \end{bmatrix}. \tag{35}$$

If all three cracks reclose, Eq. (34) is followed. In total there are 16 possible combinations of crack arrangement and appropriate changes in stress–strain relationships incorporated in solid element used in modeling bell tower. A note is output if $1 > \beta_c > \beta_t > 0$ are not true.

The transformation of $[D_c^{ck}]$ to element coordinates has the form

$$[D_c] = [T^{ck}]^T [D_c^{ck}][T^{ck}] \tag{36}$$

where $[T^{ck}]$ is transformation matrix. The open or closed status of integration point cracking is based on a strain value ε_{ck}^{ck} called the crack strain. For the case of a possible crack in the x direction, this strain is evaluated as

$$\varepsilon_{ck}^{ck} = \begin{cases} \varepsilon_x^{ck} + \frac{v}{1-v}(\varepsilon_y^{ck} + \varepsilon_z^{ck}), & \text{if no cracking has occured,} \\ \varepsilon_x^{ck} + v\varepsilon_z^{ck}, & \text{if } y \text{ direction has cracked,} \\ \varepsilon_x^{ck}, & \text{if } y \text{ and } z \text{ direction have cracked,} \end{cases} \tag{37}$$

where:

$\varepsilon_x^{ck}, \varepsilon_y^{ck}$ and ε_z^{ck} = three normal component strains in crack orientation.

The vector $\{\varepsilon^{ck}\}$ is computed by:

$$\{\varepsilon^{ck}\} = [T^{ck}]\{\varepsilon'\}, \tag{38}$$

where: $\{\text{-}\varepsilon'\}$ = modified total strain (in element coordinates)$\{\varepsilon'\}$, in turn, is defined as:

$$\{\varepsilon_n'\} = \{\varepsilon_{n-1}^{e1}\} + \{\Delta\varepsilon_n\} - \{\Delta\varepsilon_n^{th}\} - \{\Delta\varepsilon_n^{pl}\}, \tag{39}$$

where:

n = substep number;
$\{\varepsilon_{n-1}^{el}\}$ = elastic strain from previous substep;
$\{\Delta\varepsilon_n\}$ = total strain increment (based on $\{\Delta u_n\}$, the displacement increment over the substep);
$\{\Delta\varepsilon_n^{th}\}$ = thermal strain increment;
$\{\Delta\varepsilon_n^{pl}\}$ = plastic strain increment.

If ε_{ck}^{ck} is less than zero, the associated crack is assumed to be closed. If ε_{ck}^{ck} is greater than or equal to zero, the associated crack is assumed to be open. When cracking first occurs at an integration point, the crack is assumed to be open for the next iteration [33].

2.3. Mathematical formulations for static analysis

The static analysis solution method is valid for all degrees of freedom (DOFs). Inertial and damping effects are ignored, except for static acceleration fields. The overall equilibrium equations for linear static analysis are:

$$[K]\{u\} = \{F\} \tag{40}$$

or

$$[K]\{u\} = \{F^a\} + \{F^\Gamma\}, \tag{41}$$

where:

$[K]$ = total stiffness matrix = $\sum_{m=1}^{N}[K_e]$;
$\{u\}$ = nodal displacement vector;
N = number of elements;
$[K_e]$ = element stiffness matrix;
$\{F^\Gamma\}$ = reaction load vector;
$\{F^a\}$, the total applied load vector is defined by:

$$\{F^a\} = \{F^{nd}\} + \{F^{ac}\} + \sum_{m=1}^{N}(\{F_e^{th}\} + \{F_e^{pr}\}), \tag{42}$$

where:

$\{F^{nd}\}$ = applied nodal load vector;
$\{F^{ac}\} = -M\{a_c\}$ = acceleration load vector;
$[M]$ = total mass matrix = $\sum_{m=1}^{N}[M_e]$;
$[M_e]$ = element mass matrix;
$\{a_c\}$ = total acceleration vector;
$\{F_e^{th}\}$ = element thermal load vector;
$\{F_e^{pr}\}$ = element pressure load vector [33].

2.4. Mathematical formulations for modal analysis

This analysis type is used for natural frequency and mode shape determination. The equation of motion for an undamped system, expressed in matrix notation is:

$$[M]\{\ddot{u}\} + [K]\{u\} = \{0\}. \tag{43}$$

Free vibrations will be harmonic of the form:

$$\{u\} = \{\varphi\}_i \cos\omega_i t, \tag{44}$$

where:

$\{\varphi\}_i$ = eigenvector representing the mode shape of the ith natural frequency;
ω_i = ith natural circular frequency (radians per unit time);
t = time.

Thus, Eq. (43) becomes:

$$(-\omega_i^2[M] + [K])\{\varphi\}_i = \{0\}. \tag{45}$$

This equality is satisfied if either $\{\varphi\}_i = \{0\}$ or if the determinant of $([K] - \omega^2[M])$ is zero. The first option is the trivial one and, therefore, is not of interest. Thus, the second one gives the solution:

$$|[K] - \omega^2[M]| = 0. \tag{46}$$

This is an eigenvalue problem which may be solved for up to n values of ω^2 and n eigenvectors $\{\varphi\}_i$ which satisfy Eq. (45) where n is the number of DOFs.

Rather than outputting the natural circular frequencies (ω), the natural frequencies (f) are output; where:.

$$f_i = \frac{\omega_i}{2\pi}, \tag{47}$$

where: f_i = ith natural frequency (cycles per unit time) [33].

2.5. Mathematical formulations for transient analysis

The transient analysis solution method used depends on the DOFs involved. The transient dynamic equilibrium equation of interest is as follows:

$$[M]\{\ddot{u}\} + [C]\{\dot{u}\} + [K]\{u\} = \{F^a\}, \tag{48}$$

where:

$[M]$ = structural mass matrix;
$[C]$ = structural damping matrix;
$[K]$ = structural stiffness matrix;
$\{\ddot{u}\}$ = nodal acceleration vector;
$\{\dot{u}\}$ = nodal velocity vector;
$\{u\}$ = nodal displacement vector;
$\{F^a\}$ = applied load vector.

There are two main methods which can be employed for the solution of the equation: the forward difference time integration method and the Newmark time integration method. The forward difference method is used for explicit transient analysis and the Newmark method is used for implicit transient analyses and is described below.

The Newmark method uses finite difference expansions in the time interval Δt, in which it is assumed that:

$$\{\dot{u}_{n+1}\} = \{\dot{u}_n\} + [(1-\delta)\{\ddot{u}_n\} + \delta\{\ddot{u}_{n+1}\}]\Delta t, \tag{49}$$

$$\{\dot{u}_{n+1}\} = \{u_n\} + \{\dot{u}_n\}\Delta t + \left[\left(\frac{1}{2} - \alpha\right)\{\ddot{u}_n\} + \alpha\{\ddot{u}_{n+1}\}\right]\Delta t^2, \tag{50}$$

where:

α,δ = Newmark integration parameters;
$\Delta t = t_{n+1} - t_n$;
$\{u_n\}$ = nodal displacement vector at time t_n;
$\{\dot{u}_n\}$ = nodal velocity vector at time t_n;
$\{\ddot{u}_n\}$ = nodal acceleration vector at time t_n;
$\{u_{n+1}\}$ = nodal displacement vector at time t_{n+1};
$\{\dot{u}_{n+1}\}$ = nodal velocity vector at time t_{n+1};
$\{\ddot{u}_{n+1}\}$ = nodal acceleration vector at time t_{n+1}.

Since the aim is the computation of displacements $\{u_{n+1}\}$, the governing equation (48) is evaluated at time t_{n+1} as:

$$[M]\{\ddot{u}_{n+1}\} + [C]\{\dot{u}_{n+1}\} + [K]\{u_{n+1}\} = \{F^a\}. \tag{51}$$

The solution for the displacement at time t_{n+1} is obtained by first rearranging Eqs. (49) and (50), such that:

$$\{\ddot{u}_{n+1}\} = a_0(\{u_{n+1}\} - \{u_n\}) - a_2\{\dot{u}_n\} - a_3\{\ddot{u}_n\}, \tag{52}$$

$$\{\dot{u}_{n+1}\} = \{\dot{u}_n\} + a_6\{\ddot{u}_n\} + a_7\{\ddot{u}_{n+1}\}, \tag{53}$$

where:

$$a_0 = \frac{1}{\alpha \Delta t^2}, \quad a_4 = \frac{\delta}{\alpha} - 1,$$
$$a_1 = \frac{\delta}{\alpha \Delta t}, \quad a_5 = \frac{\Delta t}{2}\left(\frac{\delta}{\alpha} - 2\right),$$
$$a_2 = \frac{1}{\alpha \Delta t}, \quad a_6 = \Delta t(1-\delta),$$
$$a_3 = \frac{1}{2\alpha} - 1, \quad a_7 = \delta \Delta t.$$

Noting that $\{\ddot{u}_{n+1}\}$ in Eq. (52) can be substituted into Eq. (53) equations for $\{\ddot{u}_{n+1}\}$ and $\{\dot{u}_{n+1}\}$ can be expressed only in terms of unknown $\{u_{n+1}\}$. The equations for $\{\ddot{u}_{n+1}\}$ and $\{\dot{u}_{n+1}\}$ are then combined with Eq. (51) to form:

$$(a_0[M] + a_1[C] + [K])\{u_{n+1}\} = \{F^a\} + [M](a_0\{u_n\} + a_2\{\dot{u}_n\} + a_3\{\ddot{u}_n\}) + [C](a_1\{u_n\} + a_4\{\dot{u}_n\} + a_5\{\ddot{u}_n\}). \tag{54}$$

Once a solution is obtained for $\{u_{n+1}\}$, velocities and accelerations are updated as described in Eqs. (52) and (53).

As described by Zienkiewicz [36], the solution of Eq. (51) by means of Newmark equations (49) and (50) is unconditionally stable for:

$$\alpha \geqslant \frac{1}{4}\left(\frac{1}{2} + \delta\right)^2, \quad \delta \geqslant \frac{1}{2}, \quad \frac{1}{2} + \delta + \alpha > 0. \tag{55}$$

The Newmark parameters are related to the input as follows:

$$\alpha = \frac{1}{4}(1+\gamma)^2, \quad \delta = \frac{1}{2} + \gamma, \tag{56}$$

where: γ = amplitude decay factor.

Typically the amplitude decay factor (γ) in Eq. (56) takes a small value. The Newmark method becomes the constant average acceleration method when $\gamma = 0$, which in turns means $\alpha = \frac{1}{4}$ and $\delta = \frac{1}{2}$ [37].

Results from the constant average acceleration method do not show any numerical damping in terms of displacement amplitude errors. If other sources of damping are not present, the lack of numerical damping can be undesirable in that the higher frequencies of the structure can produce unacceptable levels of numerical noise [36]. A certain level of numerical damping is usually desired and is achieved by degrading the Newmark approximation by setting $\gamma > 0$.

The full solution method solves Eq. (54) directly and makes no additional assumptions [33].

2.6. Newton–Raphson procedure for nonlinear analysis

In nonlinear analysis, the Newton–Raphson method is employed along with the Newmark assumptions. The finite element discretization process yields a set of simultaneous equations:

$$[K]\{u\} = \{F^a\}, \tag{57}$$

where:

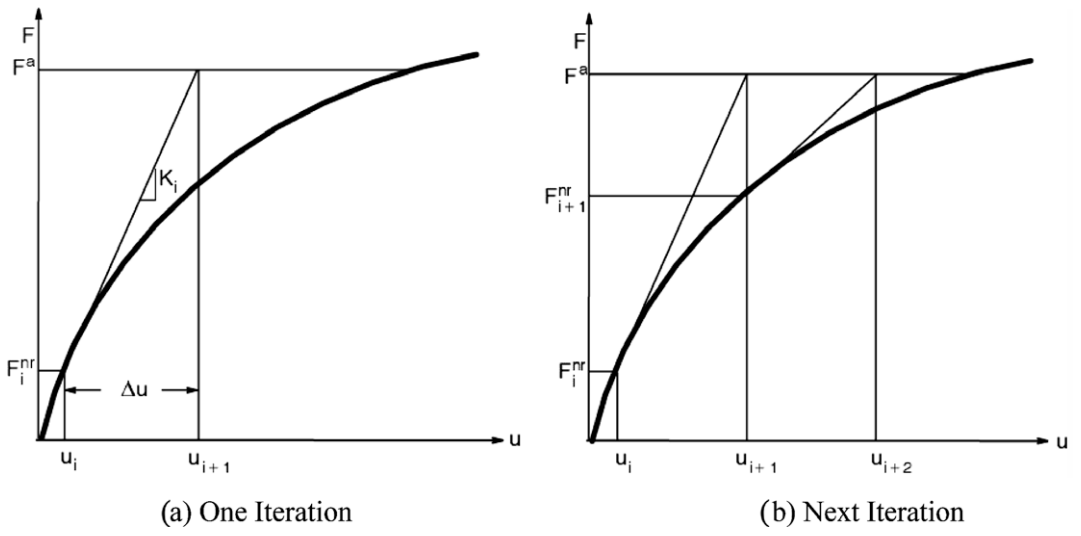

Fig. 6. Newton–Raphson solution [33].

$[K]$ = coefficient matrix;
$\{u\}$ = vector of unknown DOF (degree of freedom) values;
$\{F^a\}$ = vector of applied loads.

If the coefficient matrix $[K]$ is itself a function of the unknown DOF values (or their derivatives) then Eq. (57) is a nonlinear equation. The Newton–Raphson method is an iterative process of solving the nonlinear equations and can be written as [37]:

$$\left[K_i^T\right]\{\Delta u_i\} = \{F^a\} - \{F_i^{nr}\}, \tag{58}$$

$$\{u_{i+1}\} = \{u_i\} + \{\Delta u_i\}, \tag{59}$$

where:

$\left[K_i^T\right]$ = Jacobian matrix (tangent matrix)
i = subscript representing the current equilibrium iteration
$\{F_i^{nr}\}$ = vector of restoring loads corresponding to the element internal loads

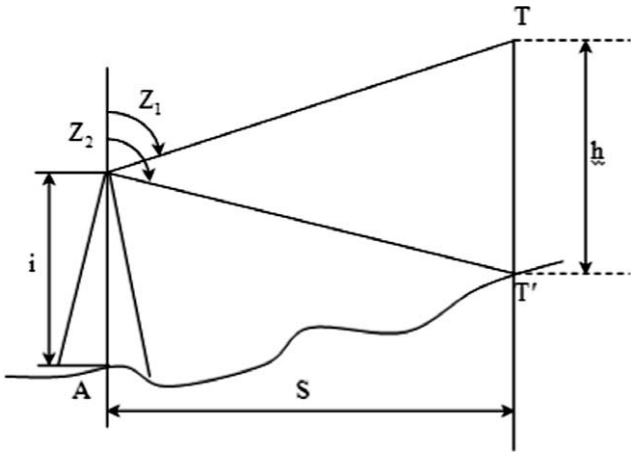

Fig. 7. Geometrical calculation notations.

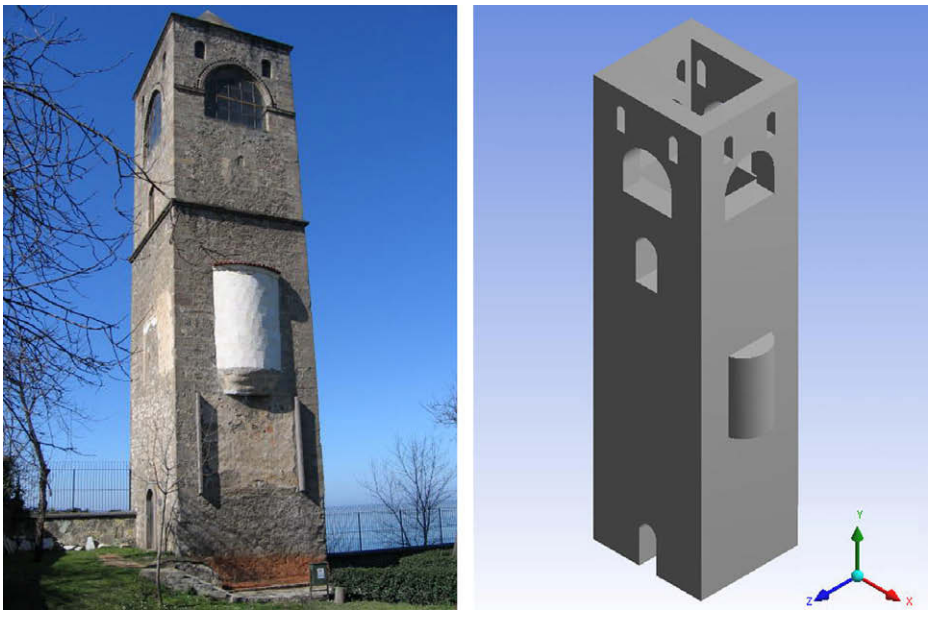

Fig. 8. Bell tower and structural solid model.

Both $\left[K_i^T\right]$ and $\{F_i^{nr}\}$ are evaluated based on the values given by $\{u_i\}$. The right-hand side of Eq. (58) is the residual or out-of-balance load vector; i.e., the amount the system is out of equilibrium. A single solution iteration is depicted graphically in Fig. 6 for a one DOF model. In a structural analysis, $\left[K_i^T\right]$ is the tangent stiffness matrix, $\{u_i\}$ is the displacement vector and $\{F_i^{nr}\}$ is the restoring force vector calculated from the element stresses. In a transient analysis, $\left[K_i^T\right]$ is the effective coefficient matrix and $\{F_i^{nr}\}$ is the effective applied load vector which includes the inertia and damping effects.

As seen in Fig. 6, more than one Newton–Raphson iteration is needed to obtain a converged solution. The general algorithm proceeds as follows:

1. Assume $\{u_0\}$. $\{u_0\}$ is usually the converged solution from the previous time step. On the first time step, $\{u_0\} = \{0\}$.
2. Compute the updated tangent matrix $\left[K_i^T\right]$ and the restoring load $\{F_i^{nr}\}$ from configuration $\{u_i\}$.
3. Calculate $\{\Delta u_i\}$ from Eq. (58).
4. Add $\{\Delta u_i\}$ to $\{u_i\}$ in order to obtain the next approximation $\{u_{i+1}\}$ (Eq. (59)).
5. Repeat steps 2–4 until convergence is obtained.

Fig. 6b shows the solution of the next iteration $(i + 1)$ of the example from Fig. 6 a. The subsequent iterations would proceed in a similar manner.

The solution obtained at the end of the iteration process would correspond to load level $\{F^a\}$. The final converged solution would be in equilibrium, such that the restoring load vector $\{F_i^{nr}\}$ (computed from the current stress state, heat flows, etc.) would equal the applied load vector $\{F^a\}$ (or at least to within some tolerance). None of the intermediate solutions would be in equilibrium [33].

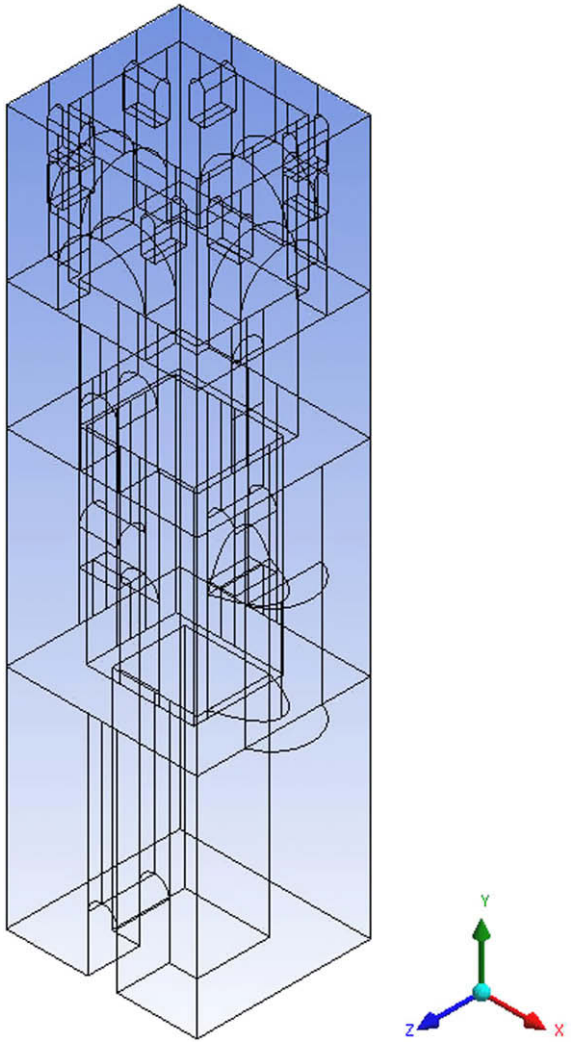

Fig. 9. General view of inside and outside.

3. Haghia Sophia bell tower

3.1. General description

This is a tall tower standing by itself at the edge of the precinct and indeed of the natural plateau, 24 m west of the west end of the church, almost on the line of its axis but very skew to it. It is nearly square in plan (5.60 m × 5.02 m) with thick stone walls and a single doorway on the south. It once had two upper stories as well as the belfry proper; presumably the floors and the access stair were all of timber. On the east face, externally, there had been a large frescoed panel contained within a stone moulding – there is now little indication of the subject of the painting which must always have been at the mercy of the weather, though part of a painted inscription and some scraps of color are still visible; even the moulding has largely broken or rotted away.

The first upper storey of the tower was a chapel; it has a very shallow apse with one small window corbelled out from its eastern wall; there are blocked windows in both north and south walls. It is this room which contains the fifteenth-century frescoes.

The wall steps back at the floor level of this chapel, as it does at each of the two upper floor levels. The chapel was vaulted and it seems possible that the access to the floors above it was from an external wooden stair. The timber beams across the top of the tower remain and probably performed the double function of acting as tie-beams for the roof construction and supports for the bells.

Externally, there is a strongly moulded string-course two-thirds of the way up the tower and above this the walls step back very slightly. There are minute windows in each of the east and south walls, above the string-course, set in the blocking of larger ones.

Fig. 10. Crack distribution in the bell tower, internal side of belfry (fourth storey).

The top level of the tower has a large pointed window in each side, now glazed, but opens of course in Byzantine times. There is a moulded string-course on the east face, at the level of arch spring, which also acts as a corbel for the voussoirs: the other windows have similar corbels at the arch springs, but no string-course. Outside the stone voussoirs the line of the arch is picked out with a row of open-ended pipes – a very effective emphasis. There are two small round-headed openings on each face just below the top of the tower.

It seems certain that this tower was a late addition to the monastery complex: not only was there a dated inscription on the painting of the Emperor Alexios IV (1417-29) on the exterior panel – this, after all, might well post-date the building of

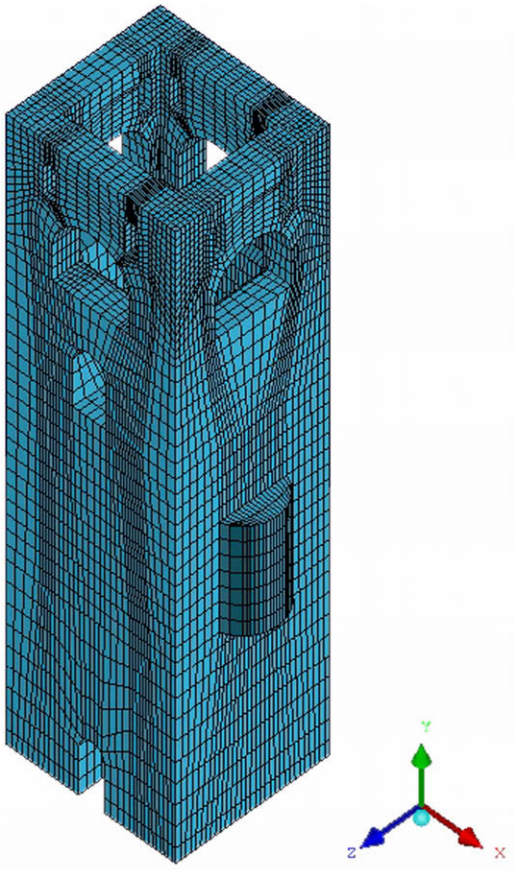

Fig. 11. The finite element mesh of the bell tower.

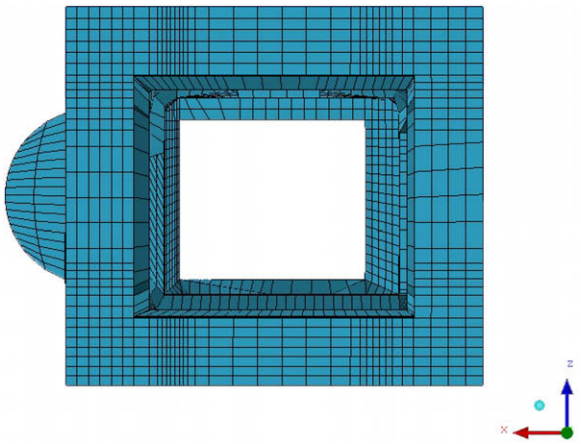

Fig. 12. The elevation view of the bell tower.

the tower – and a painted inscription inside, in the chapel, bearing the date 1443, but there is a graffito in the mortar low down on the east wall saying that the building was begun in 1427.

Recent sitework has revealed part of a vault of some earlier construction at the southeast corner of the tower. Without further excavation not much more can be said about it except that it is of different masonry from, and earlier than, the tower, since it is partially blocked by masonry identical with that of the tower.

3.2. Construction and materials

The construction of the church and bell tower is for the most part in the main Byzantine tradition, which itself is a direct descendant of Roman building methods, with modifications according to what building materials were readily available in any given area.

The materials used are stone and brick. Stone is most of the masonry work, both inside and out, is a yellowish sand–stone which weathers to a dullish grey, and was probably brought from Uniye or from a local quarry. The principal alternative stone is similar in type, but of a very much pleasanter yellowish color and which changes less with weathering. Though the whole of the interior of the structure was originally plastered, the masons went to the trouble of alternating the two different colors in the voussoirs of the internal window arches, though, as they usually started with yellow stone at the springing on each side and used an even number of voussoirs, they found themselves landed with two yellow stones together near the top.

The brick was presumably made locally, as it is now, but nothing is known of the industry in medieval Trabzon. It was used structurally, not decoratively, and much of it is therefore still hidden under plaster and whitewash in the other churches of the city. It certainly occurs in the arches of the crypt under St Anne's, and in some of the window tracery of the building in the upper castle which is often assumed to have been the great hall; but doubtless if as much cold be learnt about the structure of the other churches as has been discovered about Haghia Sophia, it would be found that brick was used structurally a great deal, though obviously it was not considered to have any aesthetic value.

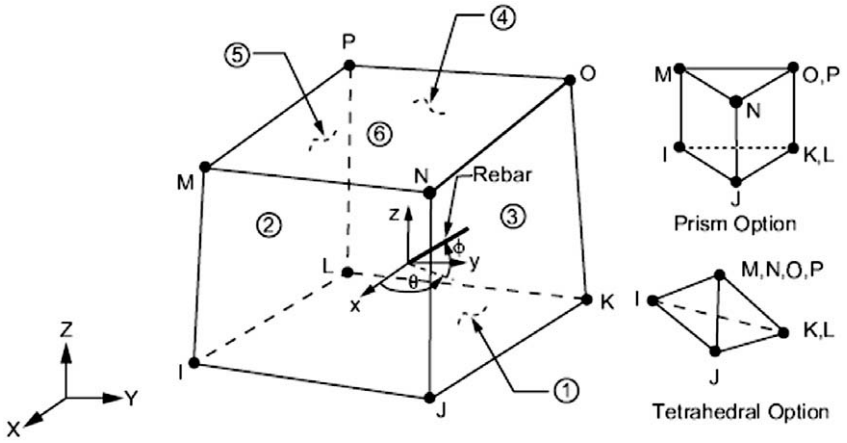

Fig. 13. Solid 65 element modeling options [38].

Table 2
Mechanical parameters adopted in the numerical analysis.

Parameter	Value
Young Modulus	5000 MPa
Poisson ratio	0.2
Density	1600 kg/m^3
Tensile strength	0.2 MPa
Compressive strength	2 MPa

Table 3
Rayleigh's damping coefficients.

ξ	Natural frequency	Rayleigh coefficients	
	ω_1	α	β
0.05	0.136	0.08545	0.117026

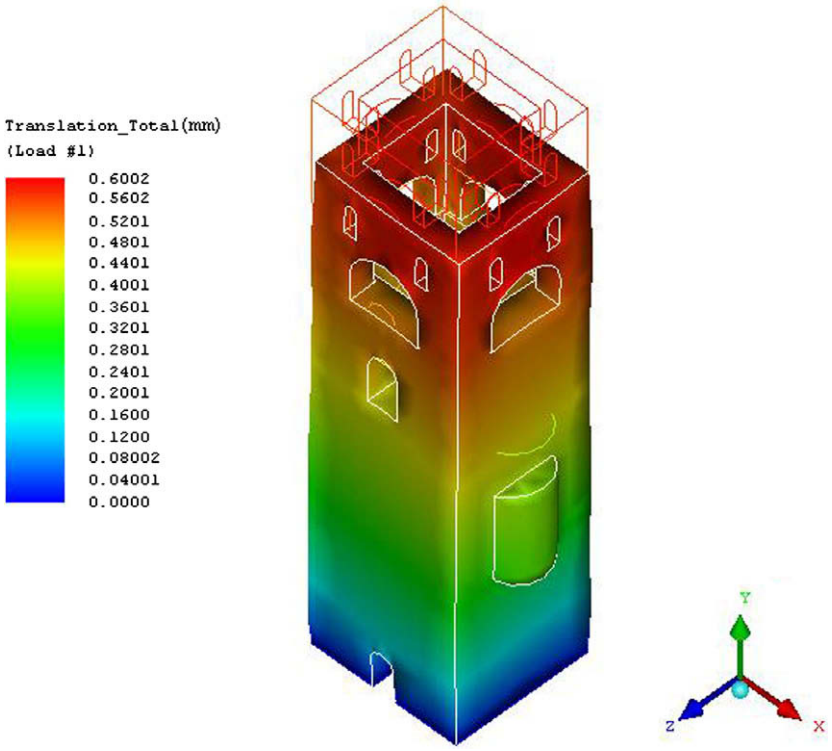

Fig. 14. Vertical displacement distribution and deformed shape of the tower due to the dead load.

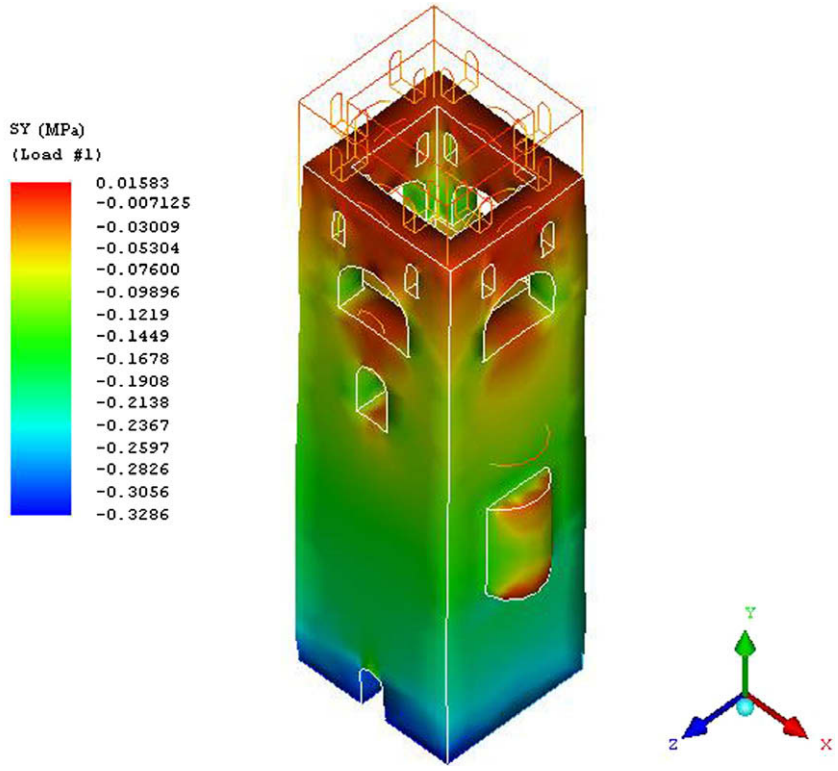

Fig. 15. Vertical stress distribution and deformed shape of the tower due to the dead load.

In general, two coats of plaster were applied – one rendering coat of lime, sand and chopped straw, and a finishing coat of lime and finer sand.

3.3. Geometrical survey

The geometry of the tower has been completely acquired and organized within a CAD system. The geodesic surveys are used to determine the dimensions of the tower. The positions of openings and the variation of the thickness of the tower with respect to that quoted have been carefully recorded.

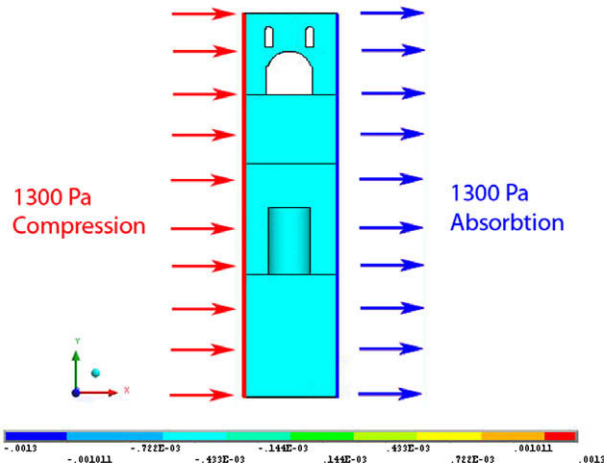

Fig. 16. Simulation of wind effect on the bell tower.

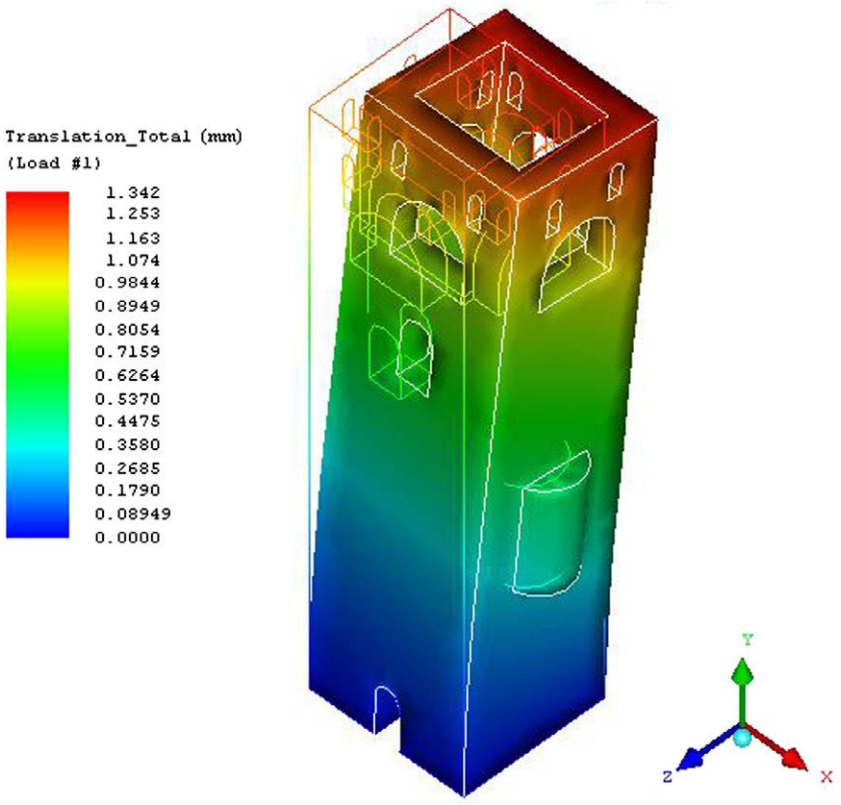

Fig. 17. Horizontal displacement distribution and deformed shape of the tower due to the wind and dead loads.

The tower detail coordinates have been measured by using Topcon total stations. The coordinates and heights of the details have been calculated by using measured horizontal lengths (S), horizontal angles and vertical angles (Z). The height of the tower has been determined by measuring the S distance between the measurement device and tower and vertical angles as shown in Fig. 7.

As shown in Fig. 7, H_A is known and Z_1,Z_2 and S are calculated by using Topcon total stations. The tower height (h) is calculated by using $h = HT - HT'$ statement as shown in Fig. 7. Firstly HT and HT' must be calculated as follows:

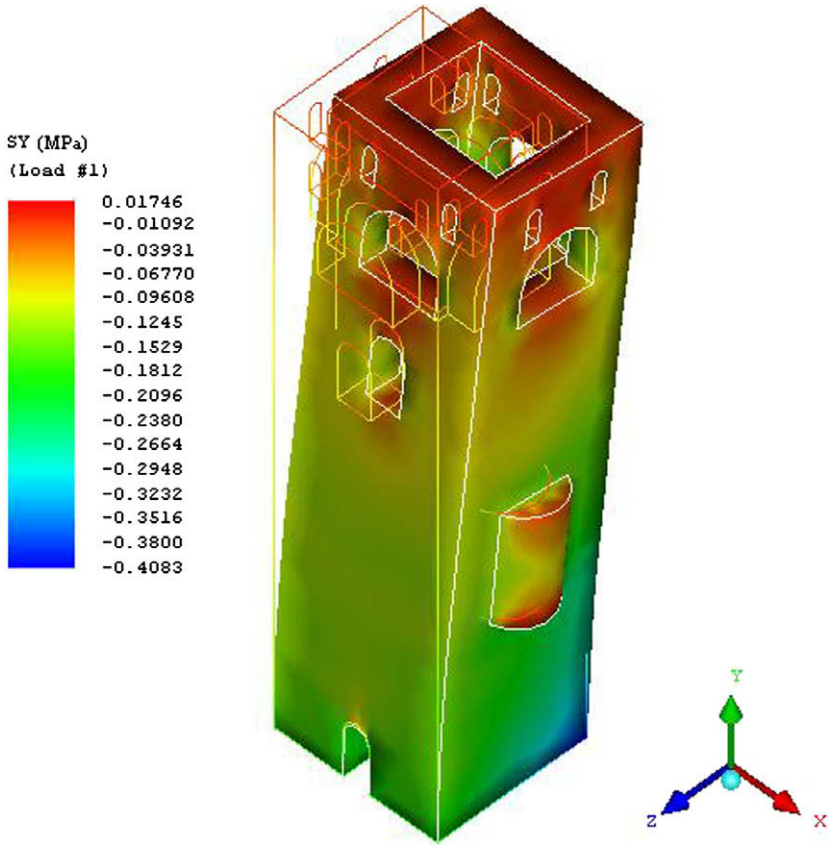

Fig. 18. Vertical stress distribution and deformed shape of the tower due to the wind and dead loads.

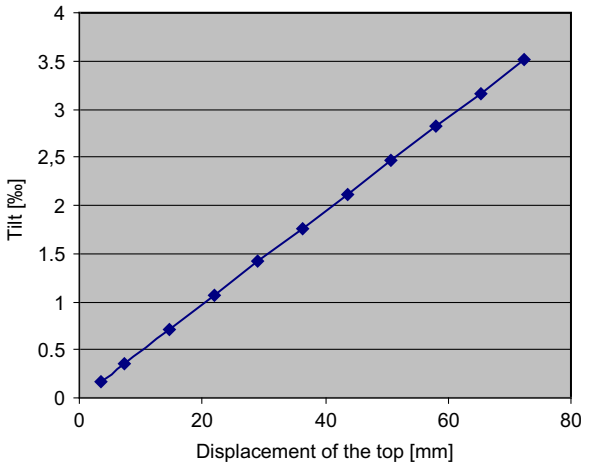

Fig. 19. Evolution of the displacement measured at the top of the tower with respect to the tilt.

$$HT = HA + S\cot(Z_1), \tag{60}$$

$$HT' = HA + S\cot(Z_2), \tag{61}$$

$$h = HT - HT' = S(\cot(Z_1) - \cot(Z_2)). \tag{62}$$

The openings inside the tower has been measured and calculated manually. The bell tower has dimensions as 5.60 m × 5.02 m in plan and its height is 20.62 m. The CAD model served as a basis for the mesh generation needed for further FEM analysis (Figs. 8 and 9).

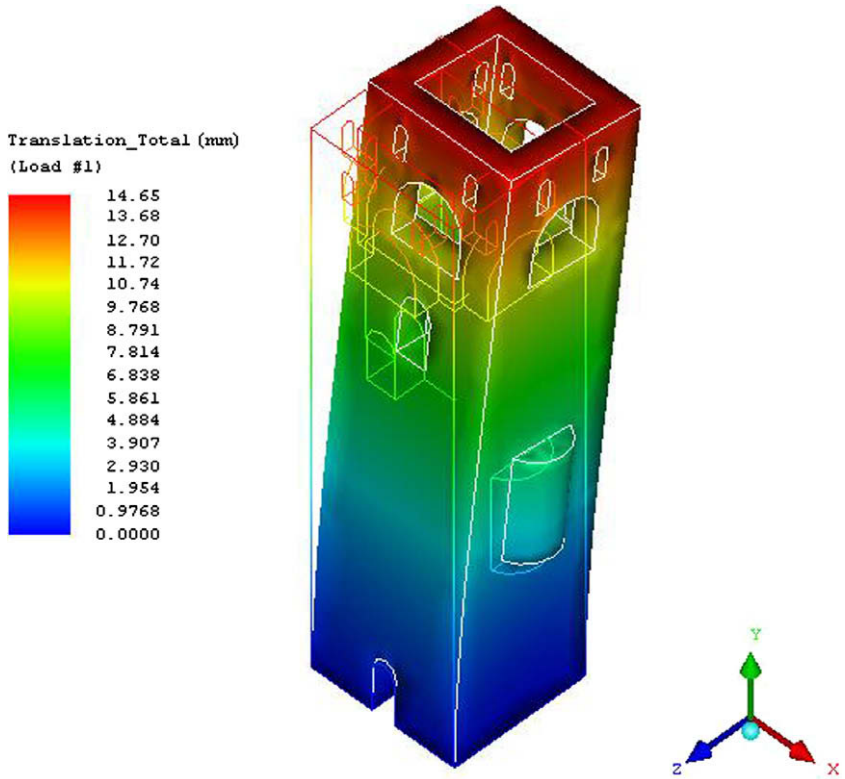

Fig. 20. Horizontal displacement distribution and deformed shape of the tower relating to a 0.71‰ tilt of the tower.

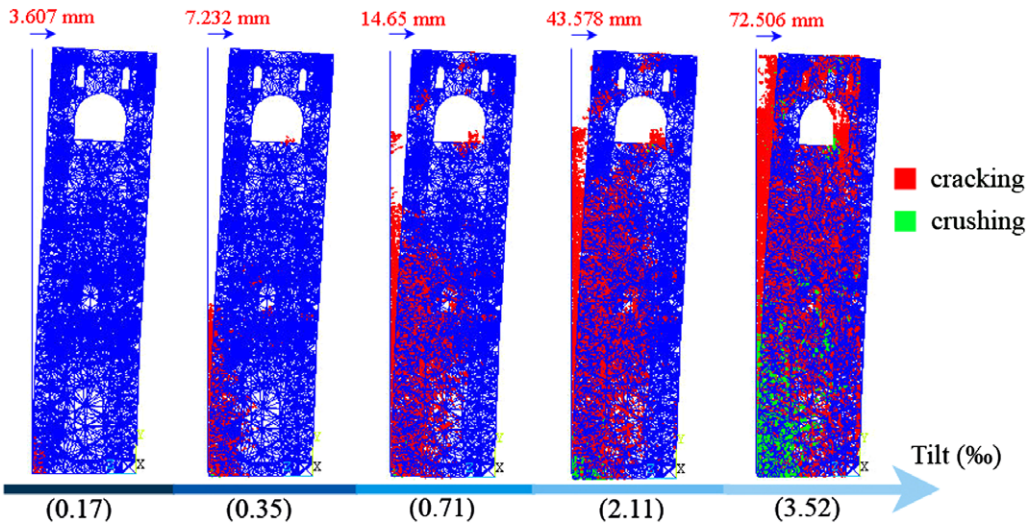

Fig. 21. Evolution of the crack distribution along the tower with respect to the tilt.

3.4. Crack distribution within the structure

The cracking network can be observed in the internal overview. The most significant cracks are inside the tower, mainly located on the fourth floor from belfry up to the top of the tower. On the external side we can observe minor cracks, mainly near the windows.

Several parts of the bell tower, particularly the fourth story of masonry structure, are in a clear state of deterioration. Internally, the facing walls of all four sides of the fourth storey of structure bear longitudinal through cracks running from

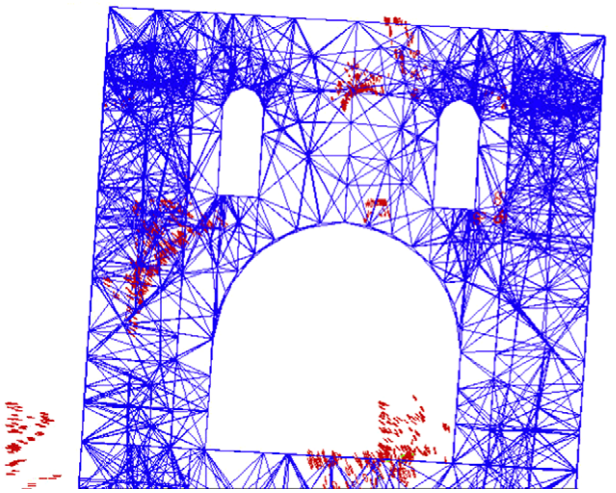

Fig. 22. Crack distribution of top storey relating to 0.71‰ tilt of the structure. (Diagonal tensile cracks occur close to the openings and micro compressive cracks start to seem about this tilt value.)

Table 4
Frequencies and periods.

Mode No.	Frequency (Hz)	Period (s)
1	4.152	0.241
2	4.570	0.219
3	12.881	0.078
4	15.982	0.063
5	17.182	0.058

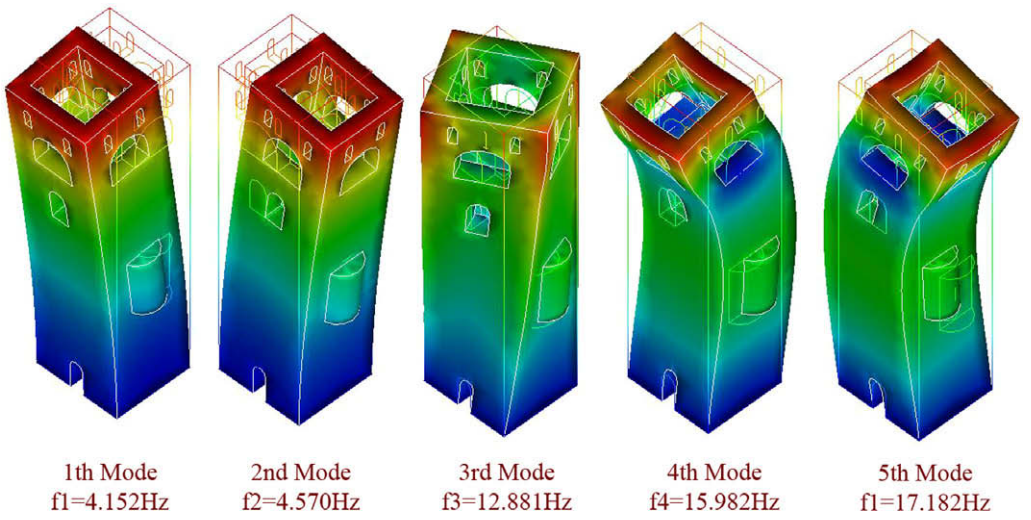

Fig. 23. The first five mode shapes and natural frequencies obtained from numerical analysis.

the base of the belfry up to the roof (Fig. 10). These cracks are clearly visible from the main windows and some of them bear the marks of previous stuccoworks testifying to their evolution over time.

Arches over doors and windows are sometimes of brick but more usually of well-cutstone voussoirs of slightly varying widths. The dressed voussoirs, present cracks, some of which have been filled with mortar and have subsequently rearranged.

The stuccowork is made from different kinds of mortar, thereby allowing the cracks to be dated to remote times. As for the belfry, wide cracks are visible in the pointed arches, at the crown, as well as in the round arches, at the haunches. Moreover, many bricks have clearly undergone detachment.

On the whole, the bell tower presents neither significant deformations, nor deviations of the edges from the vertical, nor even yielding or rotations of the structure.

4. Numerical simulation

In numerical analysis, firstly finite element model has been created depending on the geometrical and material properties of the structure. Then the optimum mesh distribution has been determined by carrying out mesh independency studies. Different mesh sizes have been tried and the mesh distribution which converges in nonlinear solution has been chosen for the model. The behavior of bell tower is determined under several different conditions. Firstly, nonlinear static analysis

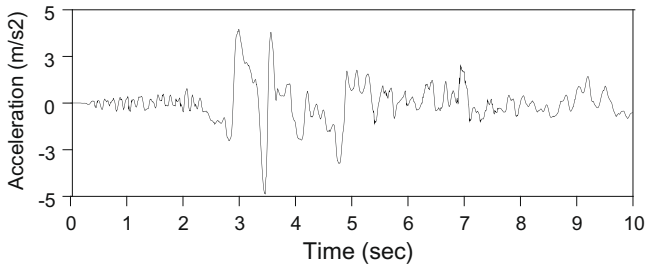

Fig. 24. East–west component of 1992 Erzincan earthquake.

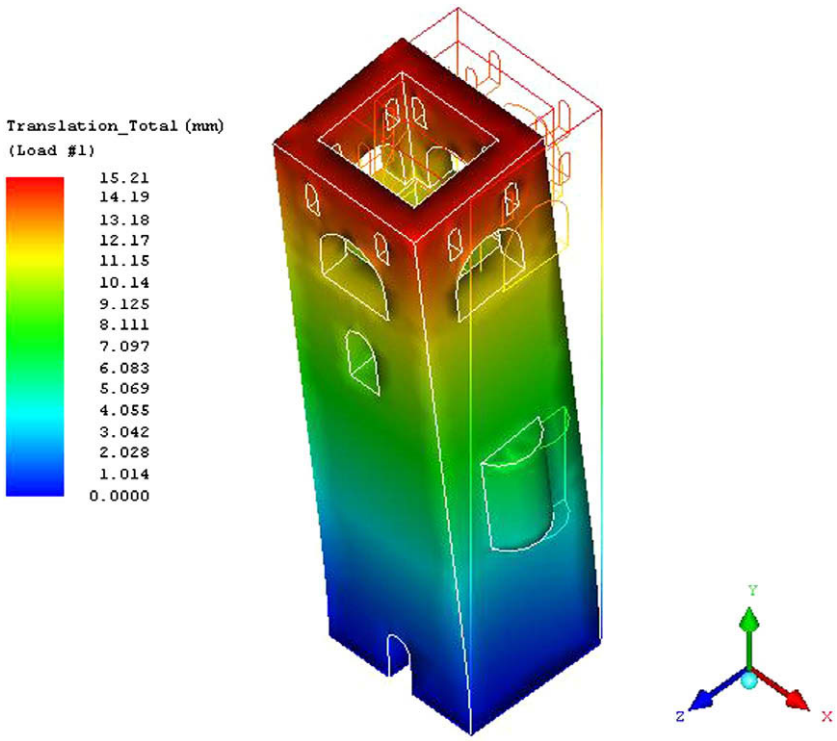

Fig. 25. Horizontal displacement distribution and deformed shape of the tower due to peak value of earthquake as $-4.86\ m/s^2$.

containing dead and wind loads has been applied to the structure. Then modal analysis and nonlinear seismic analysis have been carried out. In the nonlinear dynamic analysis, the east–west component of 1992 Erzincan earthquake is used. In addition to, an assessment of the tower's stability with respect to the tilt of the tower is carried out by means of a nonlinear analysis. Cracking and crushing of the masonry have been taken into account, as well as the influence of material nonlinearity. The numerical analysis has given a valuable picture of possible damage evolution, providing useful hints for the prosecution of structural monitoring.

4.1. 3D Finite element model

With the aim of obtaining more accurate results, a 3D finite element model was developed based on the geometrical description performed. A complete three-dimensional FEM model of the tower has been built using eight-node isoparametric solid brick elements with a uniform mass distribution. Figs. 11 and 12 show the finite element model with 9897 solid elements of the bell tower. Nonlinear static and dynamic analyses are performed by using ANSYS.

Solid65 elements [38] in Ansys library has been used for modeling the tower. The geometry, node locations and the coordinate system for this element are shown in Fig. 13. The element is defined by eight-nodes.

In numerical modeling process, all brick, prism and tetrahedral options has been used in the model. We have tried to use brick elements in modeling the tower, but because the structure does not have a smooth shape as shown in Fig. 9, most parts of the geometry has been modeled by using prism and tetrahedral options.

In order to use specific values for the mechanical characteristics of the materials of the tower, an extended in situ and laboratory experimental campaign should be carried out. Since such a campaign goes beyond the scope of the present research, typical values of the mechanical characteristics for the type of masonry involved were adopted.

For solid elements, a Young's modulus and mass density equal to 5000 MPa and 1600 kg/m^3, respectively, both for the infilled and brick masonry (Table 2) were adopted. A viscous damping coefficient, $\xi = 0.05$, was used for masonry. For time-history analyses, the Rayleigh coefficient was defined based on the first eigenvalue in the direction of maximum leaning of the tower (Table 3).

4.2. Nonlinear static analysis

For static analysis, dead and wind loads have been applied to the structure.

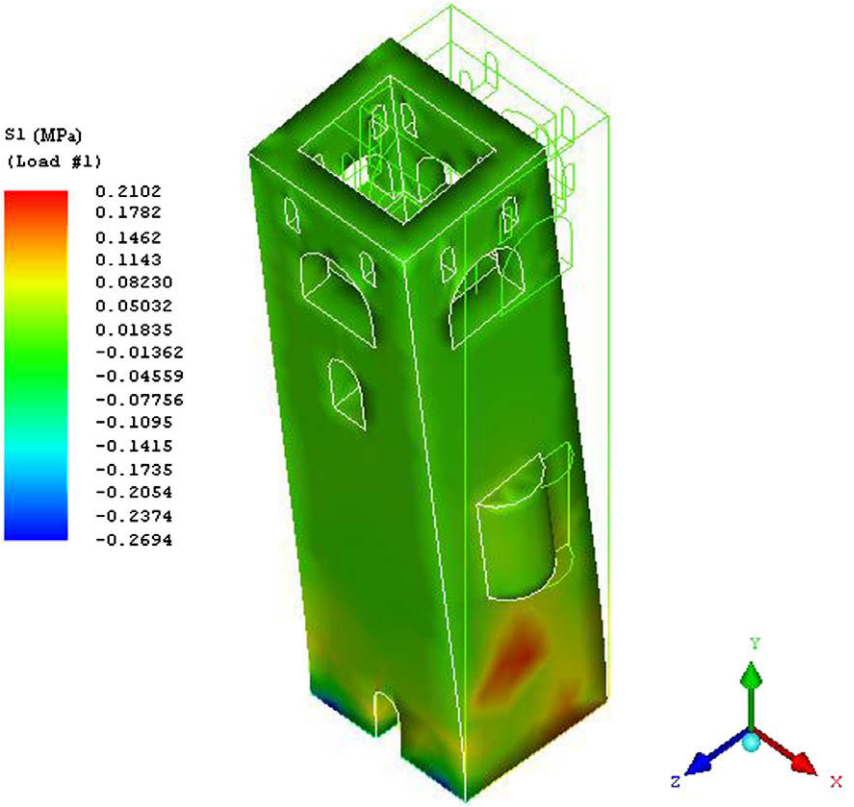

Fig. 26. Principal stress distribution and deformed shape of the tower due to negative peak value of acceleration as −4.86 m/s^2.

4.2.1. Dead load analysis

A first static analysis was performed taking into account the presence of the dead load. The vertical displacements and vertical stress distribution in the whole structure are depicted in Figs. 14 and 15.

It is seen from Fig. 14 that the max. vertical displacement is obtained as 0.6002 mm on the top of the tower. The max. compressive stress occurs at the bottom of the tower and has value of 0.32 Mpa. It is much smaller than compressive strength of masonry which is equal to 2 Mpa. For dead load analysis, no damage has been arisen through the structure.

4.2.2. Wind load analysis

The effect of wind is taken into account by means of surface pressures. Wind and dead loads have been taken into account together in the analyses. Wind loads are calculated as overpressure and underpressure acting on the tower. The magnitude of the overpressure, according to the Turkish prescriptions [39], is equal to 1300 Pa, while the underpressure is equal to 500 Pa. Both absorbtion and compression effects have been applied to the structure as overpressure effects. For the sake of simplicity, both the load distributions are assumed to be uniform as shown in Fig. 16.

The top horizontal displacement due to the wind and tower weight is approximately equal to 1.342 mm in the z-direction as shown in Fig. 17. At the base section, the maximum compressive stress is equal to approximately 0.4 MPa, much less than the yield limit assumed for the filled masonry, equal to 2 MPa as shown in Fig. 18. At the top section, the maximum tensile stress is equal to approximately 0.02 MPa, much less than the yield limit assumed for the filled masonry, equal to 0.2 MPa as shown in Fig. 18.

According to these results, there must be no crack distribution along the tower, but there are cracks as shown in Fig. 10. Therefore, we should consider tilt of the tower for proper results. For this purpose, nonlinear analysis for structural stability considering tilt of the tower has been studied.

The aim of the nonlinear analysis is to provide an assessment of the structural stability in the case of an increase in the tilt of the tower. The analysis has been carried out taking into account material nonlinearity. Material nonlinearity concerns the nonlinear stress–strain constitutive equation due to smeared cracking once the tensile strength is exceeded.

The loads are applied following a classical nonlinear incremental scheme. First of all, the dead load and the wind load were applied to the structure. At the end of this first loading step, no damage has arisen in the structure.

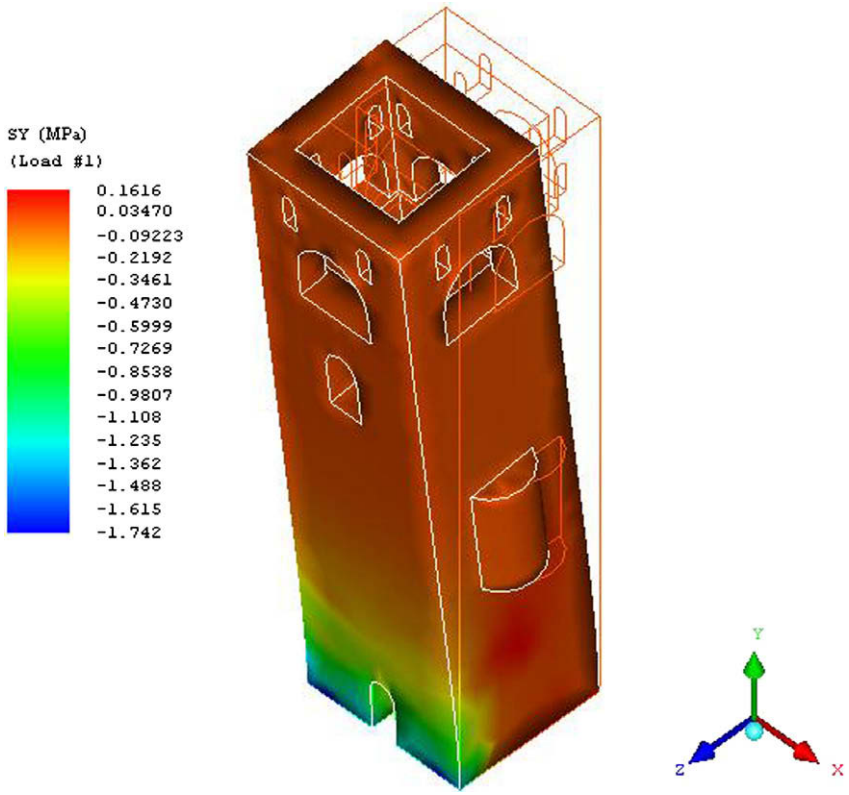

Fig. 27. Vertical stress distribution and deformed shape of the tower due to negative peak value of acceleration as $-4.86\ m/s^2$.

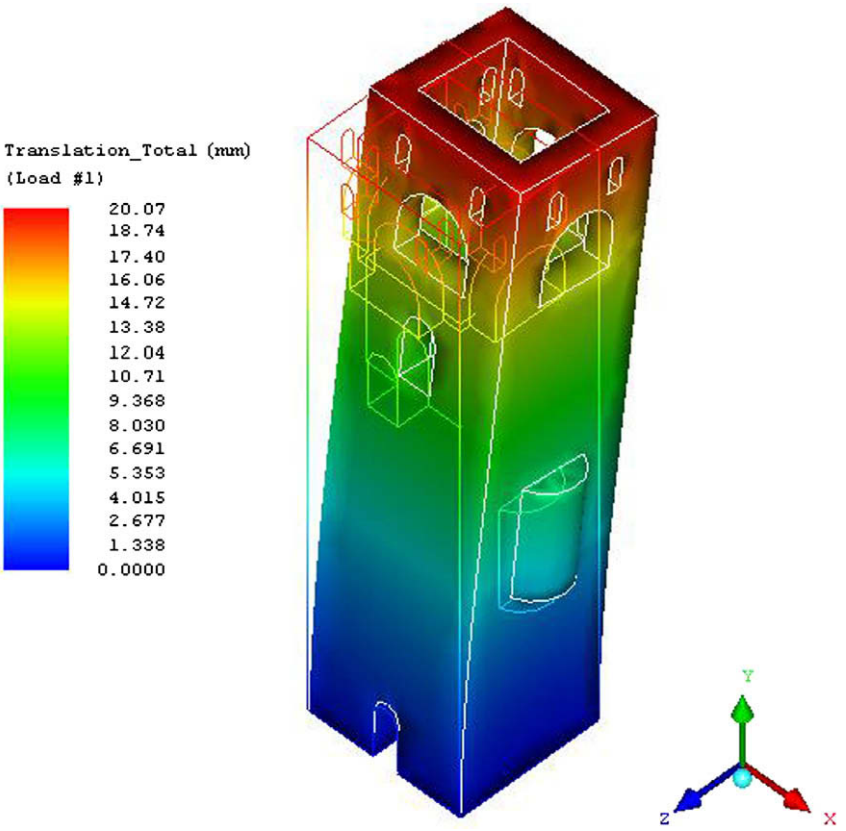

Fig. 28. Horizontal displacement distribution and deformed shape of the tower relating to a 0.71‰ tilt of the tower and peak value of acceleration as 3.95 m/s^2.

After that, the tilt is increased. The diagram in Fig. 19 shows the evolution of the calculated displacement at the top of the tower with respect to the tilt. A tilt of 0.71‰ relates to a displacement of the tower top equal to 14.65 mm as shown in Fig. 20.

The cracks occur in the model with increasing the tilt. When the tensile strength is reached, the cracks start to open as shown in Fig. 21. The region that is most sensitive to cracking is placed in the lower part of the tower.

The region that is most sensitive to crushing is placed in the bottom part of the tower because compressive stress is bigger than yield limit of masonry. When the tilt is greater than 0.71‰, also crushing of elements, due to the reaching of the ultimate compressive strength equal to 2 MPa, comes into play as shown in green colors[1] in Fig. 21.

Although the displacement of the tower top evolves almost linearly with the tilt, the damage increases in the structure. After the foundation region, the parts close to the openings in the upper segment of the tower start to crack. This can be seen in Fig. 21. Moreover, this evidence is in good agreement with present situation of the structure, which indicate the area close to the openings to be particularly sensitive to damage as seen in Fig. 22. When the tilt is greater than 0.71‰, also crushing of elements, due to the reaching of the ultimate compressive strength, comes into play. It can be concluded that the value of tilt equal to 0.71‰, and the corresponding horizontal displacement of the tower top equal to 14.65 mm, should be considered as the ultimate conditions for the structure.

4.3. Nonlinear dynamic analysis

4.3.1. Modal analysis

Preliminarily to the nonlinear analysis of the tower, a modal analysis was performed in order to determine the tower eigenvalues and eigenmodes. The frequency and period of the first 5 modes are shown in Table 4 and mode shapes are shown in Fig. 23.

[1] For interpretation of color in Fig. 21, the reader is referred to the web version of this article.

The first natural frequency is computed to be equal to 4.152 Hz, which corresponds to a period of 0.241 s. The first two modal deformations are basically connected to bending in the two orthogonal directions. The first torsional mode shape is linked to the third natural frequency, and is shown in Fig. 23.

4.3.2. Nonlinear time history analysis

One of the main problems in time history analysis is the definition of a proper input. In the case of nonlinear analyses, this is generally a ground acceleration–time history. Such time histories may be derived synthetically, by either numerical simulation of the source and wave propagation mechanisms, or by considering proper stochastic models. As an alternative, recordings of seismic events occurring on the site or on sites with similar geomorphologic characteristics, and having local effects similar to those expected for the site of the structure under exam, may be used.

As no recordings of real earthquakes are available for Trabzon, the acceleration–time histories, recorded during 1992 Erzincan Earthquake, were adopted. East–west component of 13 March 1992 Erzincan earthquake record shown in Fig. 24 is chosen for the analyses. It is observed that, due to their near locations and for the potential of their respective seismic sources, Erzincan and Trabzon cities are placed in comparable seismo-genetic areas.

The recording is applied to the structure in the direction of maximum leaning of the tower (z-axis of the model).

The analyses were carried out with ANSYS and considering a constant time integration step equal to 0.005 s. First ten seconds of the earthquake record has been used because of the computer memory problem. This includes peak acceleration values. This time history analysis results have file size which is about 65 GB. A desktop computer with 3.2 ghz processor and 4 GB RAM has been used for numerical analysis. The compute time for seismic analysis is about 15 h.

The dynamic behavior of the structure due to peak acceleration effects has been investigated for observing structure performance. The behavior of the structure can be seen in Figs. 25–27. Due to peak acceleration as -4.86 m/s^2, little tension cracks occur in the first storey walls because principal tensile stresses exceed yield limit for masonry equal to 0.2 MPa as shown in Fig. 26.

It was concluded that the value of tilt equal to 0.71‰, and the corresponding horizontal displacement of the tower top which is equal to 14.65 mm was considered as the ultimate conditions for the structure. The record also has been applied to the structure considering the value of tilt as 0.71‰.

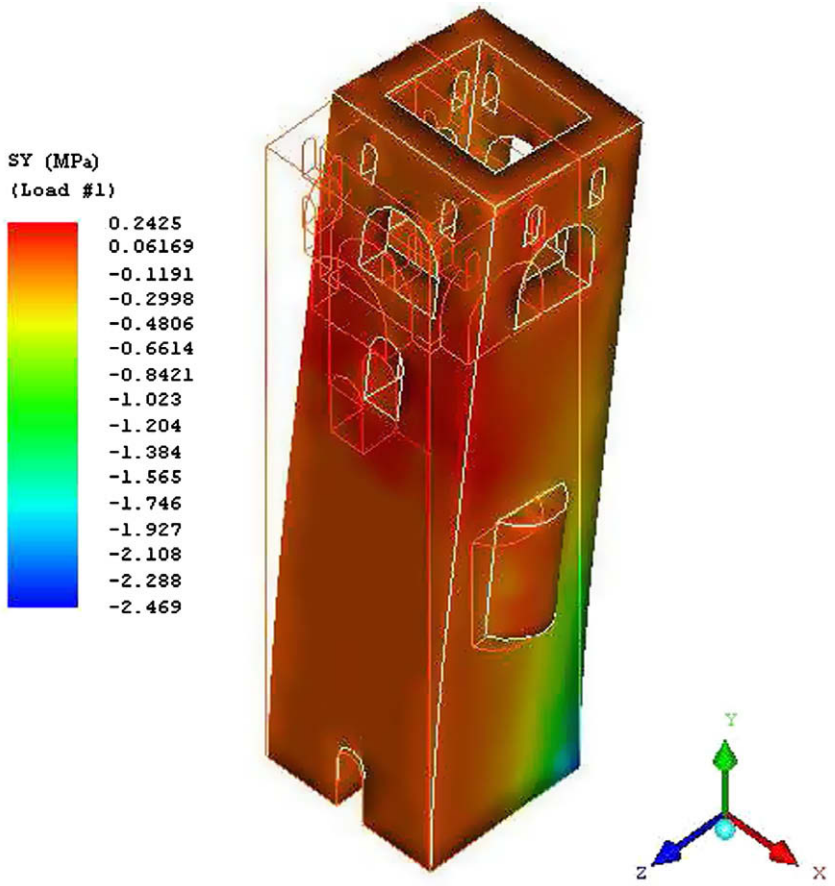

Fig. 29. Vertical stress distribution and deformed shape of the tower relating to a 0.71‰ tilt of the tower and peak value of acceleration as 3.95 m/s^2.

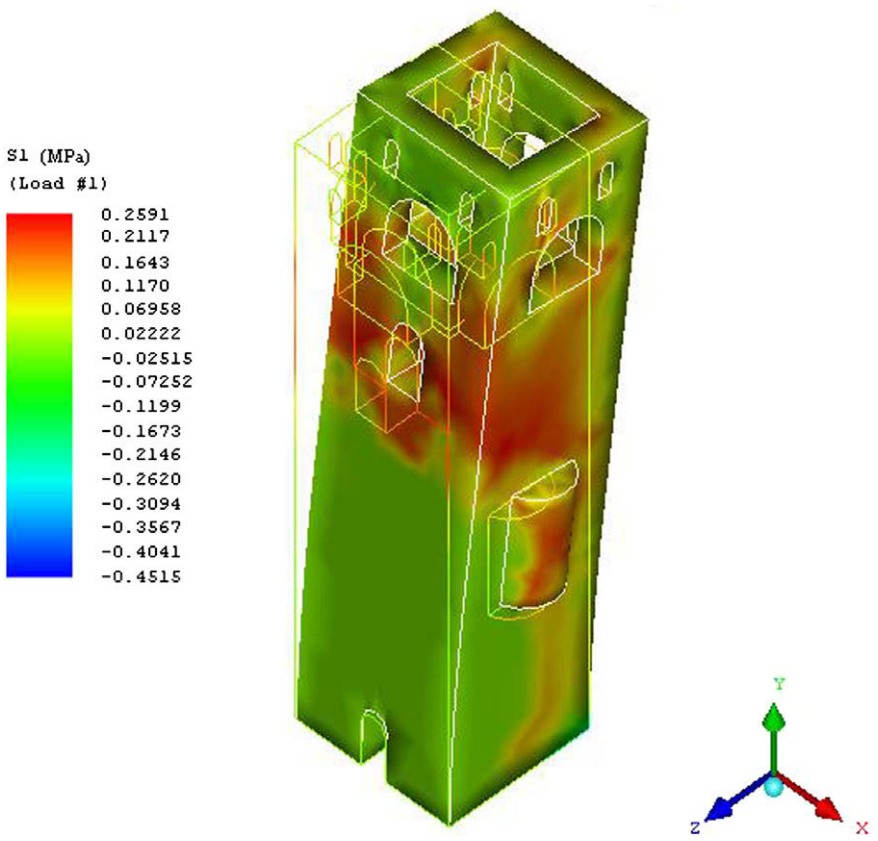

Fig. 30. Principal stress distribution and deformed shape of the tower relating to a 0.71‰ tilt of the tower and peak value of acceleration as 3.95 m/s^2.

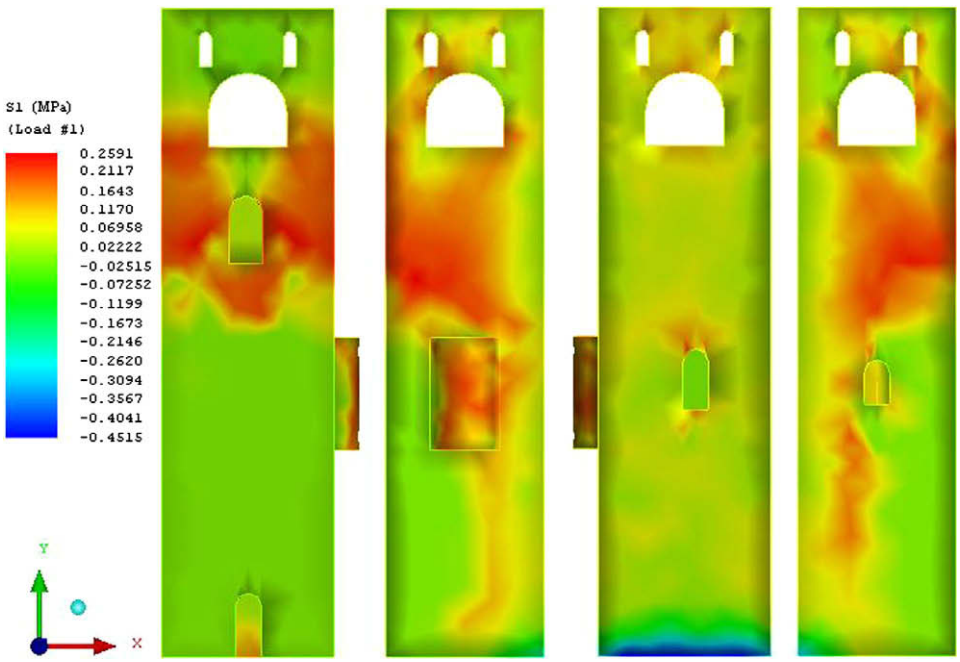

Fig. 31. Principal stress distribution of all views of tower relating to a 0.71‰ tilt of the tower and peak value of acceleration as 3.95 m/s^2.

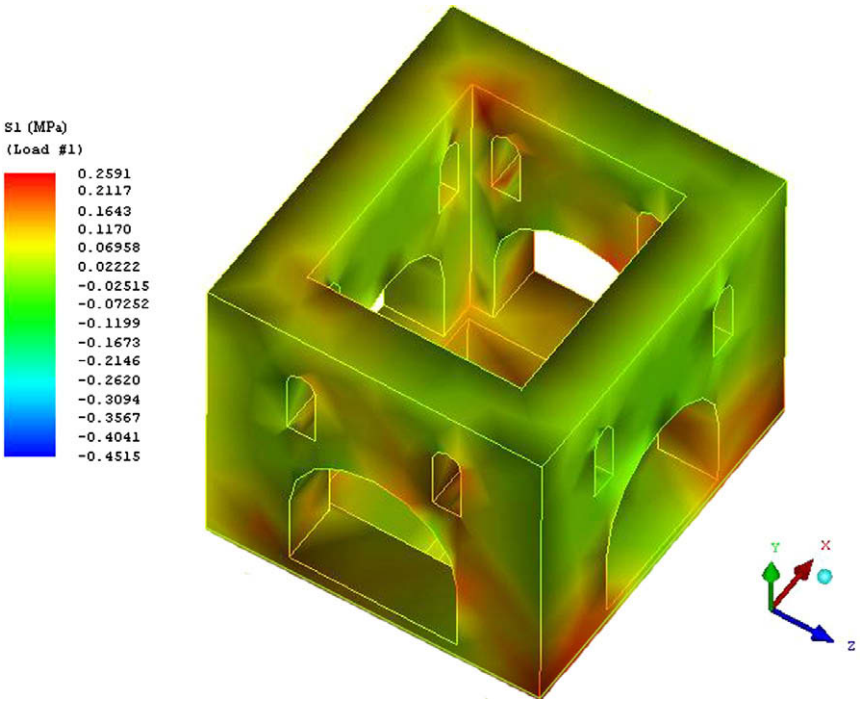

Fig. 32. Principal stress distribution of tower top storey relating to a 0.71‰ tilt of the tower and peak value of acceleration as 3.95 m/s^2 (red zones exceed tension yield limit). (For interpretation of the references to colour in this figure legend, the reader is referred to the web version of this article).

The max displacement of the tower is obtained as 20.07 mm as shown in Fig. 28. Tensile cracks occur near opening and along the upper stories because principal tensile stresses exceed yield limit for masonry equal to 0.2 MPa as shown in Figs. 29–32. And crushing occurs in bottom parts of the tower because compressive stresses increase yield limit for masonry equal to 2 Mpa as shown in Fig. 29.

5. Conclusions

A numerical damage assessment of Haghia Sophia bell tower in Trabzon, Turkey is investigated in this paper. For this purpose, nonlinear static and dynamic analyses are performed by using macro-modeling in the 3D finite element model.

Dead and wind loads are taken into account in the static analyses. Nonlinear dynamic analysis has been performed according to east–west component of the 1992 Erzincan earthquake. The results of the all analyses described in this study allow the following conclusions to be drawn:

According to analysis results due to the tower's own weight and wind, the maximum compression stress at the base of the structure is much less than the compression yield limit herein adopted for filled brick masonry and no damage has arisen in the tower.

According to analysis results due to the time history analysis, little tension cracks occur in the first storey walls, but no crushing occurs along the tower. Due to the peak acceleration and tilt of the tower, tensile cracks occur near openings and along the upper stories and crushing occurs in bottom parts of the tower.

It can be concluded that the value of tilt equal to 0.71‰ should be considered as the ultimate condition for the bell tower.

The analyses were performed by adopting material yield limits which are representative of the masonry typologies existing in the tower. Such values might, however, be quite different from the real material limits, which could be either larger or smaller than those adopted. In the latter case, the tower's behavior might be more critical than that observed in the present research. This last observation suggests that further in-depth analyses, both in situ and in the laboratory, on the mechanical behavior of the tower materials and the surrounding foundation soil, might be recommended for a more thorough evaluation of the tower vulnerability.

References

[1] J.G. Rots, Numerical simulation of cracking in structural masonry, Heron 36 (2) (1991) 49–63.
[2] G.N. Pande, J.X. Liang, J. Middleton, Equivalent elastic moduli for unit masonry, Comp. Geotech. 8 (1989) 243–265.
[3] G. Maier, E. Papa, A. Nappi, On damage and failure of unit masonry, in: Experimental and Numerical Methods in Earthquake Engineering, Balkema, Brussels and Luxembourg, 1991, pp. 223–245.

[4] P.B. Lourenço, J.G. Rots, A multi-surface interface model for the analysis of masonry structures, J. Eng. Mech., ASCE 123 (7) (1997) 660–668.
[5] H.R. Lotfi, P.B. Shing, Interface model applied to fracture of masonry structures, J. Struct. Eng. 120 (1) (1994) 63–80.
[6] G. Milani, P.B. Lourenço, A. Tralli, Homogenised limit analysis of masonry walls. Part I: Failure surfaces, Comp. Struct. 84 (2006) 166–180.
[7] G. Milani, P.B. Lourenço, A. Tralli, Homogenised limit analysis of masonry walls. Part II: Structural examples, Comp. Struct. 84 (2006) 181–195.
[8] G. Milani, P.B. Lourenço, A. Tralli, A homogenization approach for the limit analysis of out-of-plane loaded masonry walls, ASCE J. Struct. Eng. 132 (10) (2006) 1650–1663.
[9] G. Milani, P. Lourenço, A. Tralli, 3D homogenized limit analysis of masonry buildings under horizontal loads, Eng. Struct. 29 (2007) 3134–3148.
[10] A. Zucchini, P.B. Lourenço, A micro-mechanical homogenization model for masonry: Application to shear wall, Int. J. Solids Struct. 46 (2009) 871–886.
[11] A. Zucchini, P.B. Lourenço, A micro-mechanical model for the homogenization of masonry, Int. J. Solids Struct. 39 (2002) 3233–3255.
[12] A. Zucchini, P.B. Lourenço, A coupled homogenization-damage model for masonry cracking, Comp. Struct. 82 (2004) 917–929.
[13] A. Zucchini, P.B. Lourenço, Mechanics of masonry in compression: Results from a homogenization approach, Comp. Struct. 85 (2007) 193–204.
[14] P.B. Lourenço, R. de Borst, J.G. Rots, A plane stress softening plasticity model for orthotropic materials, Int. J. Numer. Meth. Eng. 40 (1997) 4033–4057.
[15] P.B. Lourenço, J.G. Rots, J. Blaauwendraad, Continuum model for masonry: Parameter estimation and validation, J. Struct. Eng., ASCE 124 (6) (1998) 642–652.
[16] P.B. Lourenço, An anisotropic macro-model for masonry plates and shells: Implementation and validation. Report no. 03.21.1.3.07, Delft University of Technology, Delft, The Netherlands/University of Minho, Guimarães, Portugal, 1997.
[17] P.B. Lourenço, Computational strategies for masonry structures, Ph.D. Thesis, 1996. <www.civil.uminho.pt/masonry>.
[18] K. Bernardeschi, C. Padovani, G. Pasquinelli, Numerical modelling of the structural behaviour of Buti's bell tower, J. Cultural Heritage 5 (2004) 371–378.
[19] A. Carpinteri, S. Invernizzi, G. Lacidogna, In situ damage assessment and nonlinear modelling of a historical masonry tower, Eng. Struct. 27 (2005) 387–395.
[20] S. Ivorra, F.J. Pallares, Dynamic investigations on a masonry bell tower, Eng. Struct. 28 (2006) 660–667.
[21] C. Modena, M.R. Valluzzi, F.R. Tongini, L. Binda, Design choices and intervention techniques for repairing and strengthening of the Monza cathedral bell-tower, Constr. Build. Mater. 16 (2002) 385–395.
[22] P. Riva, F. Perotti, E. Guidoboni, E. Boschi, Seismic analysis of the Asinelli tower and earthquakes in Bologna, Soil Dyn. Earthquake Eng. 17 (1998) 525–550.
[23] L. Binda, L. Zanzi, M. Lualdi, P. Condoleo, The use of georadar to assess damage to a masonry bell tower in Cremona, Italy, NDT& E Int. 38 (2005) 171–179.
[24] P.B. Lourenço, Assessment, diagnosis and strengthening of Outeiro Church, Portugal, Constr. Build. Mater. 19 (2005) 634–645.
[25] R.E. Klingner, Behavior of masonry in the Northridge (US) and Tecoma'n–Colima (Mexico) earthquakes: Lessons learned, and changes in US design provisions, Constr. Build. Mater. 20 (2006) 209–219.
[26] A.M. Papadopoulos, A. Avgelis, M. Santamouris, Energy study of a medieval tower, restored as a museum, Energy Build. 35 (2003) 951–961.
[27] E. Vintzileou, A. Zagkotsis, C. Repapis, C.H. Zeris, Seismic behaviour of the historical structural system of the island of Lefkada, Greece, Constr. Build. Mater. (2005).
[28] R. Cardoso, M. Lopes, R. Bento, Seismic evaluation of old masonry buildings. Part I: Method description and application to a case-study, Eng. Struct. 27 (2005) 2024–2035.
[29] R. Bento, M. Lopes, R. Cardoso, Seismic evaluation of old masonry buildings. Part II: Analysis of strengthening solutions for a case study, Eng. Struct. 27 (2005) 2014–2023.
[30] ANSYS Finite Element Analysis System, SAS IP Inc., US, 2007.
[31] A. Cecchi, G. Milani, A kinematic FE limit analysis model for thick English bond masonry walls, Int. J. Solids Struct. 45 (2008) 1302–1331.
[32] A. Cecchi, G. Milani, A. Tralli, A Reissner–Mindlin limit analysis model for out-of-plane loaded running bond masonry walls, Int. J. Solids Struct. 44 (2007) 1438–1460.
[33] Peter Kohnke (Ed.), ANSYS Inc. Theory, Release 5.7, SAS IP Inc., US, 2001.
[34] K.J. Willam, E.D. Warnke, Constitutive model for the triaxial behavior of concrete, in: Proceedings, International Association for Bridge and Structural Engineering, vol. 19, ISMES, Bergamo, Italy, 1975, p. 174.
[35] K.J. Willam, University of Colorado, Boulder, private communication, 1982.
[36] O.C. Zienkiewicz, The Finite Element Method, McGraw-Hill Company, London, 1977.
[37] K.J. Bathe, Finite Element Procedures in Engineering Analysis, Prentice-Hall, Englewood Cliffs, 1982.
[38] ANSYS Elements Reference, Release 11.0, SAS IP Inc., US, 2007.
[39] TS498, Design loads for buildings, Turkish Standard, TSI, Ankara.